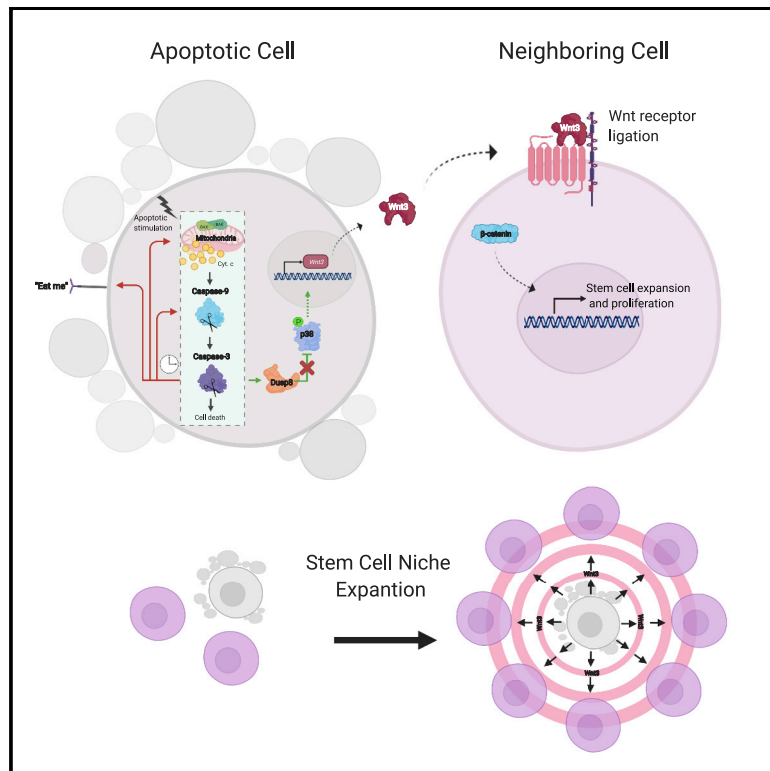


Developmental Cell

Apoptotic cells represent a dynamic stem cell niche governing proliferation and tissue regeneration

Graphical abstract



Authors

Roi Ankawa, Nitzan Goldberger, Yahav Yosefzon, ..., David J. Simon, Marc Tessier-Lavigne, Yaron Fuchs

Correspondence

yfuchs@technion.ac.il

In brief

Ankawa et al. report that deletion of *Caspase-9* in hair follicle stem cells (HFSCs) temporally delays the apoptotic cascade. These HFSCs are retained in an apoptotic-engaged state, continuously releasing Wnt3 and instructing proliferation via a caspase-3/Dusp8/p38 module. Notably, *Casp9*-deleted mice display accelerated wound repair and *de novo* hair follicle regeneration.

Highlights

- Deletion of *Caspase-9* in hair follicle stem cells delays the apoptotic cascade
- Apoptotic hair follicle stem cells release Wnt3 and instruct proliferation
- A caspase-3/Dusp8/p38 module is responsible for Wnt3 induction in apoptotic cells
- *Casp-9^{fl/fl}* mice display accelerated wound repair and *de novo* hair follicle neogenesis.

Article

Apoptotic cells represent a dynamic stem cell niche governing proliferation and tissue regeneration

Roi Ankawa,¹ Nitzan Goldberger,¹ Yahav Yosefzon,¹ Elle Koren,¹ Marianna Yusupova,¹ Daniel Rosner,¹ Alona Feldman,¹ Shulamit Baror-Sebban,² Yosef Buganim,² David J. Simon,³ Marc Tessier-Lavigne,⁴ and Yaron Fuchs^{1,5,*}

¹Laboratory of Stem Cell Biology and Regenerative Medicine, Department of Biology, Technion – Israel Institute of Technology, Haifa, Israel

²Department of Developmental Biology and Cancer Research, Institute for Medical Research Israel-Canada, the Hebrew University of Jerusalem, Hadassah Medical School, Jerusalem, Israel

³Department of Biochemistry, Weill Cornell Medical College, New York, NY 10065, USA

⁴Department of Biology, Stanford University, Stanford, CA 94305, USA

⁵Lead contact

*Correspondence: yfuchs@technion.ac.il

<https://doi.org/10.1016/j.devcel.2021.06.008>

SUMMARY

Stem cells (SCs) play a key role in homeostasis and repair. While many studies have focused on SC self-renewal and differentiation, little is known regarding the molecular mechanism regulating SC elimination and compensation upon loss. Here, we report that *Caspase-9* deletion in hair follicle SCs (HFSCs) attenuates the apoptotic cascade, resulting in significant temporal delays. Surprisingly, *Casp9*-deficient HFSCs accumulate high levels of cleaved caspase-3 and are improperly cleared due to an essential caspase-3/caspase-9 feedforward loop. These SCs are retained in an apoptotic-engaged state, serving as mitogenic signaling centers by continuously releasing Wnt3 and instructing proliferation. Investigating the underlying mechanism, we reveal a caspase-3/Dusp8/p38 module responsible for Wnt3 induction, which operates in both normal and *Casp9*-deleted HFSCs. Notably, *Casp9*-deleted mice display accelerated wound repair and *de novo* hair follicle regeneration. Taken together, we demonstrate that apoptotic cells represent a dynamic SC niche, from which emanating signals drive SC proliferation and tissue regeneration

INTRODUCTION

In many mammalian tissues stem cells (SCs) serve as a critical reservoir for replenishment and wound repair (Alonso and Fuchs, 2003; Blanpain and Fuchs, 2009; Clevers et al., 2014; Cotsarelis, 2006; Hsu et al., 2011; Tadeu and Horsley, 2014). The hair follicle (HF) houses a multitude of distinct SC populations including bulge CD34⁺ HFSCs, as well as Keratin-15 (K15)⁺ bulge and hair germ HFSCs. These SCs are responsible for driving cycles of growth (anagen), destruction (catagen), and rest (telogen) as well as facilitating skin repair (Müller-Röver et al., 2001; Soteriou and Fuchs, 2018; Cotsarelis, 2006; Cotsarelis et al., 1990; Hsu et al., 2014; Goldstein and Horsley, 2012; Morris et al., 2004; Soteriou and Fuchs, 2018; Tadeu and Horsley, 2014).

Increasing evidence now demonstrates that adult SCs utilize specific apoptotic machinery proteins for their elimination and that manipulating SC death can have significant implications (Fuchs et al., 2013; Fuchs and Steller, 2015; Koren et al., 2018; Mesa et al., 2015). In mammals, programmed cell death (PCD) serves many important functions including regulating cell numbers (Bergmann and Steller, 2010; Fuchs and Steller, 2011, 2015; Green, 2019). The best studied form of PCD is apoptosis, which is characterized by a set of morphological changes, including nuclear condensation/fragmentation, cellular

shrinkage, mRNA decay, and membrane blebbing (Green, 2019; Kerr et al., 1972; Singh et al., 2019; Tuzlak et al., 2016). Apoptosis can be induced intrinsically by intracellular signaling and extrinsically by ligation of death ligands (Fuchs and Steller, 2015; Peltzer and Walczak, 2019; Tait and Green, 2013; Vanden Berghe et al., 2014; Walczak, 2011). During apoptosis, permeabilization of mitochondria results in release of cytochrome *c*, which binds the adaptor protein apoptotic protease-activating factor 1 (Apaf-1) and caspase-9 (Hu et al., 2014; Kim et al., 2005). The resulting complex, called the apoptosome, leads to cleavage and activation of caspase-9, which plays a key role in mediating the initial apoptotic signal and the execution of cellular suicide (Donepudi and Grütter, 2002; Hakem et al., 1998; Kuida et al., 1998; Rehm et al., 2006; Stennicke and Salvesen, 2000).

For many years, apoptosis was considered a silent process that does not affect the neighboring environment, (Bergmann and Steller, 2010; Damgaard and Gyrd-Hansen, 2011; Fuchs and Steller, 2015; Gyrd-Hansen and Meier, 2010; Ichim and Tait, 2016). However, elegant studies in *Drosophila* have shown that apoptotic cells can release mitogenic factors that drive proliferation of neighboring cells in a process termed apoptosis-induced-proliferation (AiP) (Fan and Bergmann, 2008; Fogarty and Bergmann, 2017; Fogarty et al., 2016; Martín et al., 2009; Morata et al., 2011; Pérez-Garijo et al., 2004; Ryoo and

Bergmann, 2012; Ryoo et al., 2004). AiP has since been shown to play a role in different organisms (Chera et al., 2009; Huang et al., 2011; Kurtova et al., 2015; Li et al., 2010). However, the extrinsic effects of a dying SC during mammalian homeostasis and regeneration remain poorly characterized.

Given the vital role of HFSCs in organ maintenance and repair, we evaluated the role of apoptosis in HFSCs. We found that the initiator caspase-9 is highly expressed in HFSCs. To circumvent lethality of whole-body deletion of *caspase-9* (*Casp9*) (Hakem et al., 1998; Kuida et al., 1998), we generated a *Casp9* floxed (*Casp9^{fl/fl}*) mouse that harbors a *Krt15*-specific inducible Cre recombinase. We demonstrate that caspase-9 is a key mediator of K15⁺ HFSC apoptosis and that its deletion attenuates the execution of the apoptotic program. Intriguingly, *in vivo*, caspase-9-deficient cells accumulate high active levels of caspase-3 *in vivo*. However, caspase-3 activation is not sufficient for rapid HFSC elimination due to an essential caspase-3/caspase-9 feedforward loop. Consequently, these SCs are retained in an apoptotic-engaged state, during which they release mitogenic Wnt3 to their surroundings. Investigating the underlying mechanism, we found that caspase-3 cleaves dual specificity phosphatase 8 (Dusp8), thereby enhancing the activation of p38-Mapk, which induces *Wnt3* transcription to promote HFSC niche expansion. Importantly, *Casp9*-deleted mice display accelerated wound repair and *de novo* HF regeneration.

Taken together, we reveal a critical role of caspase-9 as a central regulator of apoptotic kinetics. We report that the rate required for SC death and, as a derivative, the persistence of this Wnt3 releasing niche can have pronounced effects on skin homeostasis and regeneration.

RESULTS

Caspase-9 is highly expressed in the HFSC niche

To elucidate the specific apoptotic machinery proteins utilized by mouse HFSCs (Figure 1A), we sorted integrin $\alpha 6^{+}$ CD34⁺ Scal⁻ HFSCs (henceforth denoted CD34⁺) and integrin $\alpha 6^{+}$ CD34⁻ Scal⁺ epidermal stem/progenitor cells, as we previously described (Kostic et al., 2017; Soteriou et al., 2016). We next compared the expression profile of different members of the caspase family via RNA-seq. Interestingly, the initiator caspase-9 was relatively highly expressed in the CD34⁺ HFSCs (Figure 1B), unlike the initiator caspases-2 and -8 (Lin et al., 2004). Given the enrichment of *Caspase-9* (*Casp9*) transcript in CD34⁺ HFSCs, we examined caspase-9 protein levels in skin wholemounts. Immunofluorescence for the procaspase-9 zymogen revealed high amounts in the bulge of telogenic (P56) tail and dorsal HFs (Figures 1C, S1A, and S1B). Next, we examined the activation of caspase-9 using a specific antibody that detects only the cleaved form. In accordance with our previous findings (Fuchs et al., 2013; Yosefzon et al., 2018), we find that caspase-9 can become activated in the bulge and hair germ (Figure S1C).

Deletion of *Casp9* results in expansion of the HFSC niche

Since our results indicated that caspase-9 is abundant in HFSCs, we examined the effect of deleting *Casp9*. Since whole-body deletion of *Casp9* causes embryonic lethality (Hakem et al.,

1998; Kuida et al., 1998), we engineered and generated a conditional *Casp9* mouse model (denoted *Casp9^{fl/fl}*) floxed at exon 6 encompassing the catalytic region (QACGG) of the protein (Figures S1D–S1F). As *Casp9* was found to be expressed in both bulge and hair germ HFSCs, we selected the conditional and inducible *B6;SJL-Tg(Krt15-cre/PGR)22Cot/J* mouse line (henceforth denoted *K15-Cre^{PGR}*), which would specifically drive the deletion in both compartments. To generate the conditional knockout (denoted *K15-Cre^{PGR}/Casp9^{fl/fl}*), we crossed *Casp9^{fl/fl}* mice to *K15-Cre^{PGR}* mice that also harbor a *Rosa26-EYFP* cassette, thereby enabling fluorescent labeling of enhanced yellow protein (EYFP) upon Cre recombination (Figure S1G). Administration of RU486 resulted in successful deletion of *Casp9* specifically in bulge and hair germ HFSCs (Figure 1D). Moreover, a large majority of EYFP⁺ cells (88%) were negative for *Casp9* (Figures 1D and S1H). To investigate the consequence of *Casp9* deletion, we administered RU486 to telogenic (P56) mice and examined dorsal skin HFSC expansion after a 1-week chase. We found that deletion of *Casp9*, after only one week, led to expansion of CD34⁺ and K15⁺ HFSC populations (Figures 1E and 1F). While *Casp9*-deleted HFs displayed overall normal morphology, the sizes of the bulge and hair germ had increased (Figures 1G and 1H). To quantify HFSC numbers we performed flow cytometry, which revealed a 2-fold increase in the number of CD34⁺ HFSCs upon *Casp9* deletion (Figure 1I). *Casp9^{fl/fl}*-dependent phenotypes were consistent in the tail skin, which displayed significantly more EYFP⁺ cells in *Casp9^{fl/fl}* mice (Figures S1I and S1J). Notably, we detected a similar ratio of EYFP⁺ and EYFP⁻ HFSCs comparing *K15-Cre^{PGR}* and *K15-Cre^{PGR}/Casp9^{fl/fl}* HFs (Figure 1J). These results show that deletion of *Casp9* for a short interval is sufficient for driving cell expansion in the bulge. Additionally, we examined the effect of *Casp9* deletion for a longer time frame of 6 months post-induction (Figure 1K). Our data indicate increased bulge size and increased numbers of both EYFP⁺ and EYFP⁻ HFSCs, indicating that expansion is not limited to *Casp9*-deleted cells (Figures 1K and 1L).

Caspase-9 loss delays apoptosis and clearance of HFSCs

Since deletion of *Casp9* led to HFSC expansion, we next examined whether it is mediated by acquired resistance to apoptosis. We induced telogenic (P56) mice with RU486 and performed terminal deoxynucleotidyl transferase dUTP nick end labeling (TUNEL), which marks double-stranded DNA breaks generated during apoptosis. Our data indicate a 4-fold decrease in the amount of condensed TUNEL⁺ cells in the bulge and hair germ of *Casp9^{-/-}* mice. (Figures 2A and S2A).

We next verified these findings *in vitro* utilizing CD34⁺ HFSCs transduced with H2B-reporter lentiviral vectors encoding shRNA control (shCtrl) or shRNA *Casp9* (shCasp9). Knockdown efficiency of *Casp9* mRNA (~95%) was determined by real-time PCR (Figure S2B). First, we examined apoptotic resistance in shCtrl and shCasp9 HFSCs upon exposure to staurosporine (STS). In contrast to shCtrl cells, shCasp9 HFSCs displayed significantly less TUNEL staining (Figures S2C and S2D).

The key characteristics of an apoptotic cell include nuclear condensation and membrane blebbing (Kerr et al., 1972). Hence, we utilized time-lapse imaging of shCtrl and shCasp9 H2B-GFP⁺ reporter cells, monitoring nuclei size upon STS administration. In

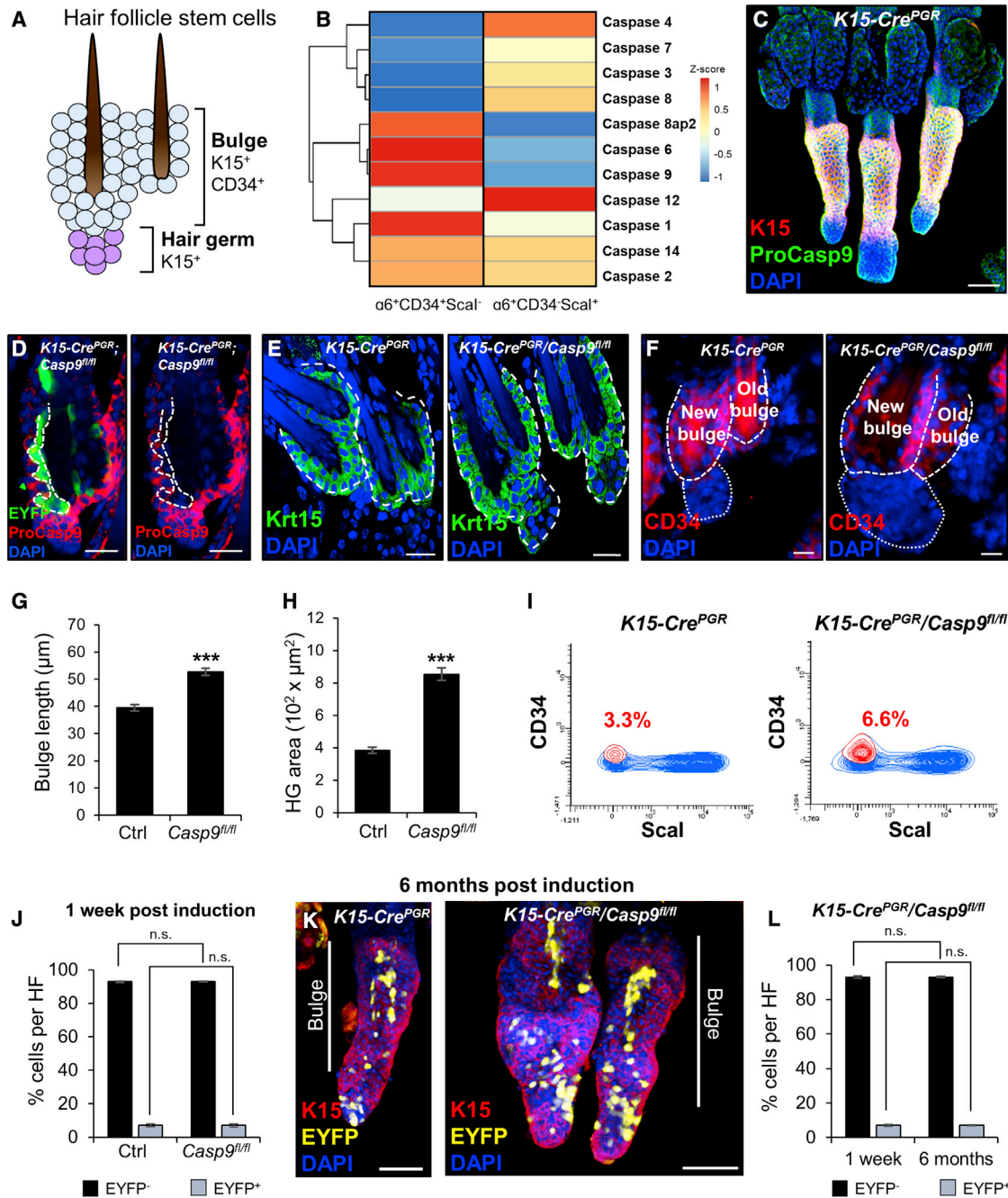


Figure 1. Loss of *Casp9* in HFSCs leads to SC niche expansion

(A) Schematic of mouse telogenic dorsal HF.
 (B) Heatmap comparing caspase expression levels.
 (C) Immunostaining of telogenic tail HF for keratin-15 (K15) and procaspase-9.
 (D) Immunostaining for procaspase-9 and EYFP in *K15-Cre^{PGR}/Casp9^{fl/fl}* dorsal bulge. Dashed line marks EYFP⁺ cells.
 (E and F) Immunostaining of telogenic dorsal HF stained for K15 (E) and CD34 (F).
 (G and H) Quantifications of dorsal bulge length and hair germ area 1-week post-induction.
 (I) Flow cytometry of CD34⁺ cells from integrin- $\alpha 6^+$ /Scal⁻ epidermal pool (n = 3 pooled mice).
 (J) Quantification of EYFP⁺ cells in *K15-Cre^{PGR}* and *K15-Cre^{PGR}/Casp9^{fl/fl}* mice 1-week post-induction.
 (K) Tail HF from *K15-Cre^{PGR}* and *K15-Cre^{PGR}/Casp9^{fl/fl}* mice 6 months post-induction stained for K15 and showing EYFP induction.
 (L) Quantification of EYFP⁺ cells in *K15-Cre^{PGR}/Casp9^{fl/fl}* mice comparing 1 week and 6 months post-induction.
 Images are representative of n = 3 mice and n = 50 to 100 HF. Error bars represent \pm SEM. Scale bars: 50 μ m (C, E, F, and K), 20 μ m (D).
 See also Figure S1.

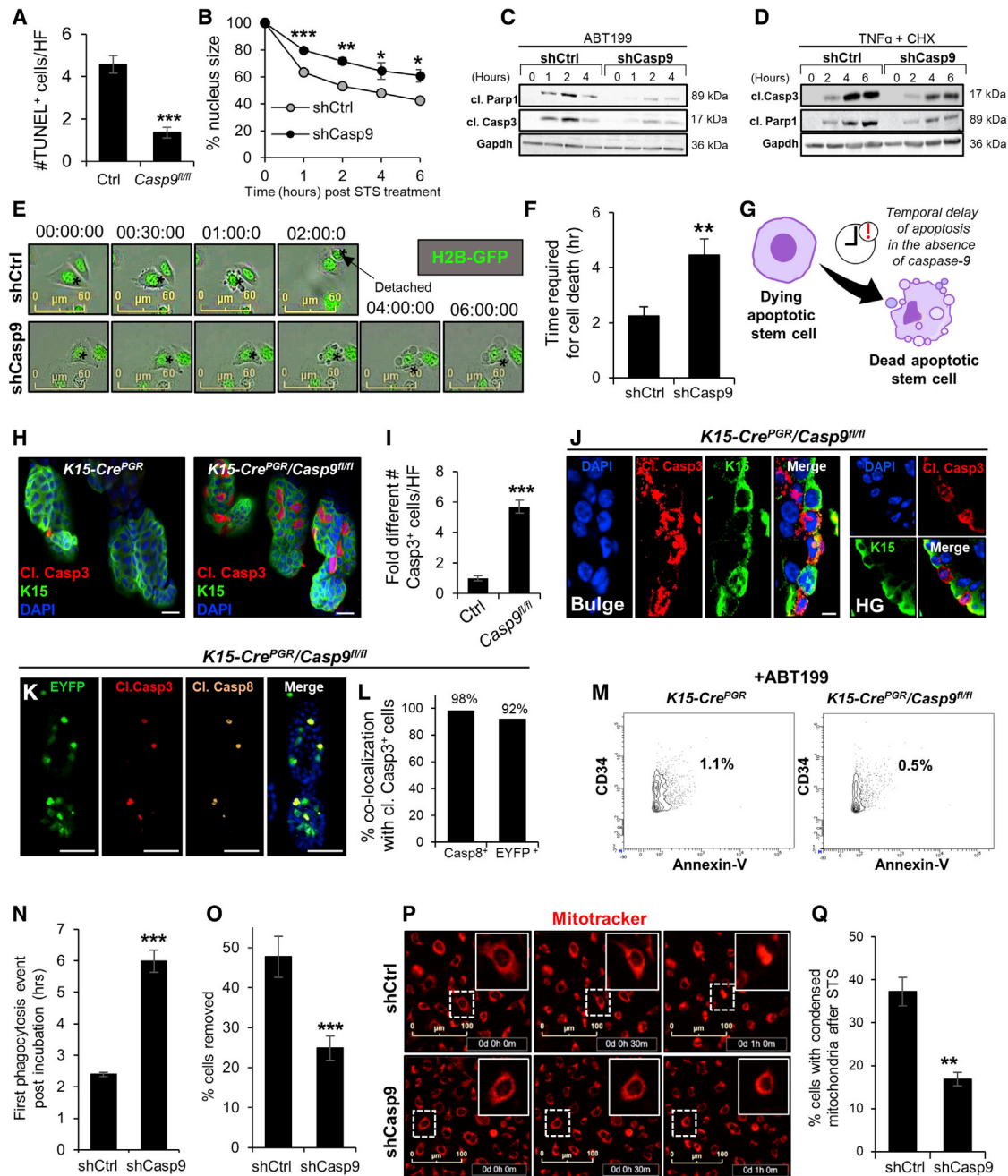


Figure 2. Caspase-9 loss delays apoptosis and clearance of HFSCs

(A) Quantification of TUNEL⁺ cells per HF.
 (B) Quantification of nuclei size of shCtrl and shCasp9 cells upon STS treatment.
 (C and D) Immunoblot for cleaved caspase-3, cleaved Parp1, and Gapdh upon ABT199 (C) or TNF- α /cycloheximide (D).
 (E) Time-lapse images of non-treated single dying shCtrl and shCasp9 cells.
 (F) Quantification of time required for cell death.
 (G) Schematic of temporal apoptotic delay in caspase-9-deficient cells.
 (H) Telogenic dorsal HF^s stained for cleaved caspase-3 and K15.
 (I) Quantification of cleaved caspase-3⁺ in the hair follicle.
 (J) Co-labeling of cleaved caspase-3 and K15 in bulge (left) and HG (right) in dorsal HF^s.
 (K) Immunostaining of cleaved caspase-3 and caspase-8 with EYFP induction in telogenic HF^s.
 (L) Co-localization of cleaved caspase-8 and EYFP with cleaved caspase-3 in telogenic HF^s.
 (M) Flow cytometry showing annexin V⁺ cells from integrin- α 6⁺/CD34⁺ population.
 (N) Quantification of first phagocytosis event.

(legend continued on next page)

contrast to control HFSCs, caspase-9-silenced cells significantly preserved their nuclei size (Figures S2E and S2F). In shCtrl HFSCs, the size of nuclei diminished to ~60% after just 1 h, while shCasp9 HFSCs maintained ~80% size (Figure 2B). This trend was significant throughout all examined time points (Figure 2B; Video S1). These results suggest that silencing of caspase-9 can attenuate apoptotic kinetics. In support of these findings, we found that cleavage of the downstream apoptotic hallmark, Parp1, was significantly delayed upon silencing of caspase-9 during STS stimulation (Figure S2G).

Immunoblotting against cleaved caspase-3, the downstream apoptotic target of caspase-9, revealed a similar pattern as for cleaved Parp1, indicating delayed apoptotic kinetics (Figure S2H). Next, we verified these findings utilizing more specific and physiologically relevant apoptotic stimulators. Similar to our previous results, administration of either the Bcl-2 inhibitor ABT199 or TNF- α /cycloheximide resulted in a similar trend for cleaved caspase-3 and cleaved Parp1 (Figures 2C, 2D, S2I, and S2J; Video S2).

To further validate these findings, we utilized time-lapse imaging of untreated cells, where control cells displayed rapid initiation of membrane blebbing and nuclear condensation upon commitment to the apoptotic process (Figure 2E; Video S3). In contrast, shCasp9 HFSCs started to exhibit the morphological hallmarks after 2 h: a time frame in which control cells had detached from the plate. We found that dying shCasp9 cells were retained in an apoptotic state for significantly longer time than the control (Figures 2E and 2F; Video S3).

Taken together, these findings indicate that caspase-9 is required for temporal execution of apoptosis and that its depletion causes delayed apoptotic timing (Figure 2G).

We next examined the activation of caspase-3 *in vivo*. Surprisingly, we found that the *Casp9*-deficient HFSC niche encompassed a relatively large number of cleaved caspase-3⁺ HFSCs in contrast to control (Figures 2H and 2I). In these HFSCs, caspase-3 appeared functional as demonstrated by cleavage and elimination of K15, which is a reported caspase-3 target (Figure 2J; Badock et al. 2001). Nevertheless, the wide majority of active caspase-3⁺ cells appeared relatively normal and did not exhibit membrane blebbing, nuclear condensation or fragmentation in contrast to regular apoptotic HFSCs (Figure S2K). To evaluate whether these cells were functionally destined to be eliminated, we performed co-staining of cleaved caspase-3 and TUNEL in *K15-Cre^{PGF}/Casp9^{fl/fl}* mice. Although the number of TUNEL⁺ cells decreased in the *Casp9*-deficient HFSC niche, we found that all TUNEL⁺ cells exhibited high levels of cleaved caspase-3 (Figure S2L and S2M).

We also detected increased levels of cleaved caspase-8 upon deletion of *Casp9*, offering an explanation as to how caspase-3 could still become active in the absence of caspase-9 (Figures S2N and S2O; Stennicke et al. 1998). To evaluate whether caspase-8 was active in *Casp9^{fl/fl}* cells that displayed activate cas-

pase-3, we co-stained *K15-Cre^{PGF}/Casp9^{fl/fl}* (P56) skin whole-mounts with antibodies against cleaved caspase-3 and caspase-8. Our results indicate that almost all cleaved caspase-3⁺ cells (98%) were also positive for cleaved caspase-8. Notably, most of the co-labeled active caspase-3⁺/-8⁺ cells were EYFP positive (92%), indicating that active caspase-8 can activate caspase-3 in the absence of caspase-9 (Figures 2K and 2L). To further test this, we treated shCtrl and shCasp9 HFSCs with ABT199 and evaluated caspase activity at sequential time points. Following apoptotic stimulation, we found that cleaved caspase-8 levels corresponded to the rise in cleaved caspase-3 levels (Figure S2P). In this setting, we also observed a delay in the activation of caspase-3 and -8 in the absence of caspase-9, in accordance with our previous results.

These findings raise two interconnected questions: (1) why is there an increase in cleaved caspase-3⁺ cells *in vivo* upon *Casp9* deletion (versus the delay *in vitro*) and (2) how can the lack of caspase-9 prevent caspase-3 from reaching the required threshold for cell elimination?

To address the first question, we investigated whether the increase in cleaved caspase-3⁺ cells could arise due to a clearing defect. This critical aspect in apoptosis is facilitated by the exposure of phosphatidylserine (PS) on the extracellular surface of the cell, which serves as a signal for engulfment and clearing of the apoptotic cell (Henson, 2017; Nagata, 2018). Thus, we examined the effect of *Casp9* deletion *in vivo* on the exposure of PS following treatment with ABT199, by staining for annexin V, which binds PS on the outer leaflet. Flow cytometry indicated that in the absence of caspase-9, HFSCs displayed a significant decrease in the exposure of PS (Figure 2M). We next verified these findings *in vitro* by both immunofluorescence and flow analyses using both STS and ABT199 stimuli. Our results established that upon caspase-9 silencing, cells displayed a decrease in the exposure of PS during all examined time points (Figures S3A–S3C).

A critical step in PS exposure is facilitated by the phospholipid ATP11C flippase, which becomes cleaved and inhibited during apoptosis (Segawa et al., 2014). Through immunoblotting we detected a strong decrease in the cleavage products of ATP11C upon caspase-9 silencing (Figure S3D). These results provide an explanation for the decrease in PS exposure, highlighting a crucial role of caspase-9 in this process and shed light on why cleaved caspase-3⁺ HFSCs were not efficiently cleared from the bulge. Furthermore, we also examined the presence of the apoptotic repelling “do not eat me” signal CD47. Flow cytometry revealed a rapid decrease in CD47 levels in shCtrl HFSCs following stimulation with ABT199 (Figure S2E). In contrast, shCasp9 displayed only a modest decrease in the levels of CD47 (Figure S2E).

Taking a complementary approach to monitor the clearance defect upon caspase-9 loss of function we also performed functional phagocytosis assays. For this aim, we stimulated both

(O) Quantification of cells cleared during a 12-h efferocytosis assay.

(P) Snapshots of cells treated with STS and labeled with MitoTracker.

(Q) Quantification of cells displaying condensed mitochondrial morphology after 1 h of STS.

Images are representative of n = 3 mice, ≥ 3 culture triplicates or 100 HFSCs. Error bars represent \pm SEM. Scale bars: 100 μ m (P), 60 μ m (E), 50 μ m (K), 20 μ m (H), and 5 μ m (J).

See also Figures S2 and S3.

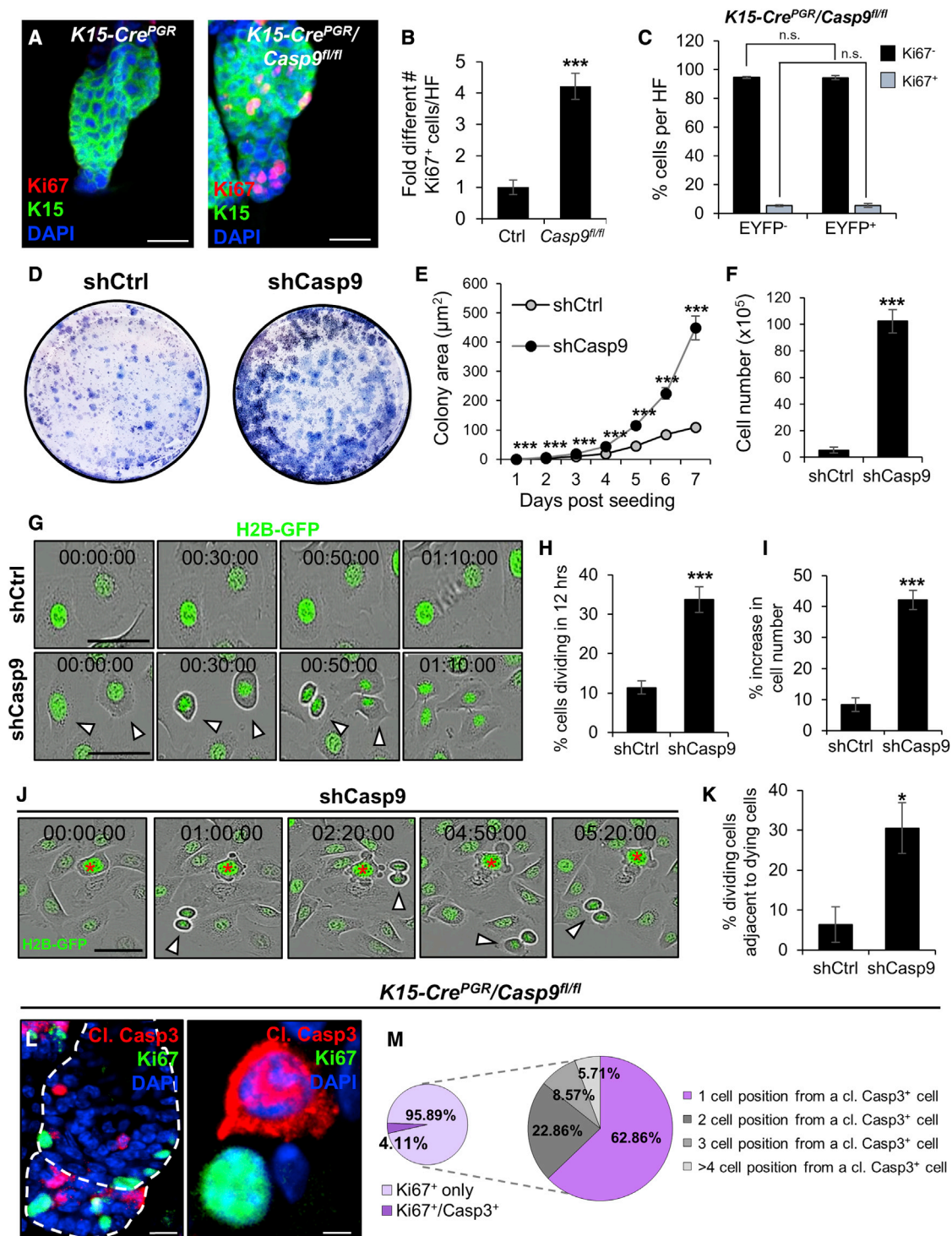


Figure 3. Deletion of *Casp9* results in increased proliferation of HFSCs

(A) Immunostaining of telogenic dorsal HFSCs stained for Ki67 and K15.
 (B) Quantification of Ki67⁺ cells in the HF.
 (C) Ratio of Ki67⁺ cells in EYFP⁺ and EYFP⁻ populations.
 (D) Rhodanile staining of HFSC colonies 8 days post-plating.
 (E) Quantification of colony size.
 (F) Quantification of cell number after 24 h of live imaging.
 (G) Time-lapse images of HFSCs during mitosis. Arrowheads point to cell division events.

(legend continued on next page)

shCtrl and shCasp9, administered ABT199 for a short interval, and added APC-labeled macrophages (RAW264.7). In control cells the first phagocytosis event could be seen as early as 2 h post-apoptotic induction, whereas shCasp9 underwent phagocytosis after 6 h post-induction (Figure 2N). These findings are in line with times required for cell death and membrane blebbing (Figure 2E). Furthermore, the number of cleared cells was significantly lower upon caspase-9 silencing (Figure 2O; Video S4).

We next examined why cleavage and activation of caspase-3 was insufficient for rapid elimination of the *Casp9^{fl/fl}* HFSCs. Previously, it has been proposed that an amplification loop of caspase-3 with what is considered “upstream” apoptotic events is required for execution of the full-blown apoptotic response (Lakhani et al., 2006; McComb et al., 2019). Mitochondrial outer membrane permeabilization (MOMP) is considered the “point of no return” in the apoptotic cascade, which is an event regulated by the executioner caspase-3 and caspase-7 (Lakhani et al., 2006). We therefore hypothesized that, since cells appeared relatively normal and caspase-3 appeared functional, caspase-3 could not generate the feedforward loop required for mitochondrial collapse. To examine this, we performed time-lapse imaging of mitochondria utilizing the MitoTracker dye. Our data indicate that in control HFSCs, the mitochondria become fragmented and condensed after 1 h of STS exposure (Figures 2P and 2Q; Video S5). In contrast, *Casp9*-silenced cells did not exhibit this morphological feature at this time point. Upon MOMP, cytochrome *c* is released from the mitochondria (Tait and Green, 2013). To evaluate this event, we performed mitochondrial fractionation on shCtrl and shCasp9 cells treated with STS for increasing time points. Immunoblotting revealed that shCtrl cells secrete cytochrome *c* in increasing levels as STS exposure increases, while shCasp9 cells maintained steady cytochrome *c* levels (Figure S3F). We reasoned that if indeed caspase-3 functions “upstream” in HFSCs it could also affect the activation of caspase-9. To assess this possibility, we next utilized *Casp3^{-/-}* mice. We isolated telogenic (P56) tail skins and could detect the cleavage of caspase-9 in control (WT) mice, in accordance with our previous findings (Yosefzon et al., 2018). In mice deficient for *Casp3* we could not detect the activation of caspase-9 within the HF (Figures S3G–S3I). These data suggest that caspase-3 generates a feedforward loop required for complete elimination of a HFSC. Taken together, our results indicate that caspase-9 plays a critical role in regulating apoptotic kinetics of HFSCs, serving as one explanation for the observed expansion of the HFSC pool.

Deletion of *Casp9* results in increased HFSC proliferation

Amplified cell proliferation of *Casp9^{fl/fl}* HFSCs could be an alternative explanation to the observed increase in expansion potential. To examine this, we administered RU486 to telogenic (P56)

mice and harvested dorsal skins after 1 week when mice were still in telogen (Müller-Röver et al., 2001). In control mice we could barely detect any proliferating HFSCs, as expected from a quiescent phase of the HF. Intriguingly, deletion of *Casp9* resulted in a significant increase in the number of Ki67⁺ proliferative bulge and hair germ HFSCs (Figures 3A and 3B). In accordance with our previous findings, the Ki67 increase was evident in both EYFP⁺ and EYFP⁻ HFSCs (Figure 3C).

Proliferation in the HF usually represents the induction of anagen (Alonso and Fuchs, 2006). Therefore, we next examined whether the absence of caspase-9 in HFSC, which drives HFSC proliferation, would alter the HF cycle. Induced telogenic *K15-Cre^{PGR}* and *K15-Cre^{PGR}/Casp9^{fl/fl}* mice exhibited telogenic morphology at 1- and 3 weeks post-induction (Figures 1D, 1E, and S4A–S4C), indicating that HFSC proliferation in this setting does not result in early entry to anagen. Furthermore, we performed waxing experiments to initiate anagen on the dorsal skin post-induction (Müller-Röver et al., 2001). Both control and *Casp9*-deficient HFs displayed similar morphology and skin darkening after 8 days, indicative of anagen (Figures S4D–S4F).

To examine whether effects on HFSC proliferation could be niche dependent, we examined the effect of caspase-9 silencing *in vitro*. We first cultured shCtrl and shCasp9 cells and examined their expansion. Analyzing the expansion of our cultures, we found that silencing of caspase-9 resulted in an increase in the number of cells and size of holoclones (Figures 3D–3F, S4G, and S4H). After 1 week in culture, the average size of individual colonies expanded 4.5 times, with more overall colonies and an increase in cell number by almost 20-fold over the course of the experiment (Figures 3D–3F). Immunostaining against Ki67 indicated that shCasp9 HFSCs proliferate ~2.5 times more than shCtrl cells (Figures S4I and S4J). We next performed live imaging *in vitro*, which verified our Ki67 results and indicated that shCasp9 HFSCs proliferate significantly more than shCtrl cells (Figures 3G and 3H; Video S6). Within a 10-h window, we found that ~10% of control HFSCs underwent mitosis. In contrast, ~40% of shCasp9 HFSCs began cycling (Figure 3I). We did not find any change in the period required for mitosis in both cultures (Figure S4K). Thus, our data indicate that the number of cells proliferating, but not the duration of the cell cycle, is affected by caspase-9 silencing.

We noted that in many cases proliferating cells were seen adjacent to cells undergoing apoptosis. This phenomenon was significantly more pronounced in shCasp9 HFSCs, presumably as they exhibited attenuated apoptotic kinetics and were not properly cleared (Figures 3J and 3K; Video S7). Apoptosis in HFSC cultures is a relatively frequent event in uninduced conditions as we have previously shown (Fuchs et al., 2013). To examine whether caspase-3⁺ HFSCs were located near proliferating cells in *Casp9^{fl/fl}* mice *in vivo*, we performed co-labeling

(H and I) Quantification of cells dividing (H) and number (I) in a 12-h time frame.

(J) Images of shCasp9 cells. Red asterisk demarks dying cell adjacent to a dividing cell (arrowhead).

(K) Percentage of cells dividing adjacent to dying cells.

(L) Immunostaining of dorsal telogenic HF against Ki67 and cleaved caspase-3. Right panel: zoom in on bulge cells.

(M) Positional quantification of Ki67⁺ cells with respect to cleaved caspase-3⁺ cells.

Images are representative of $n = 3$ mice, ≥ 3 culture triplicates or 30–100 HFs. Error bars represent \pm SEM. Scale bars: 50 μ m (A, G, and J), 2 μ m (L).

See also Figure S4.

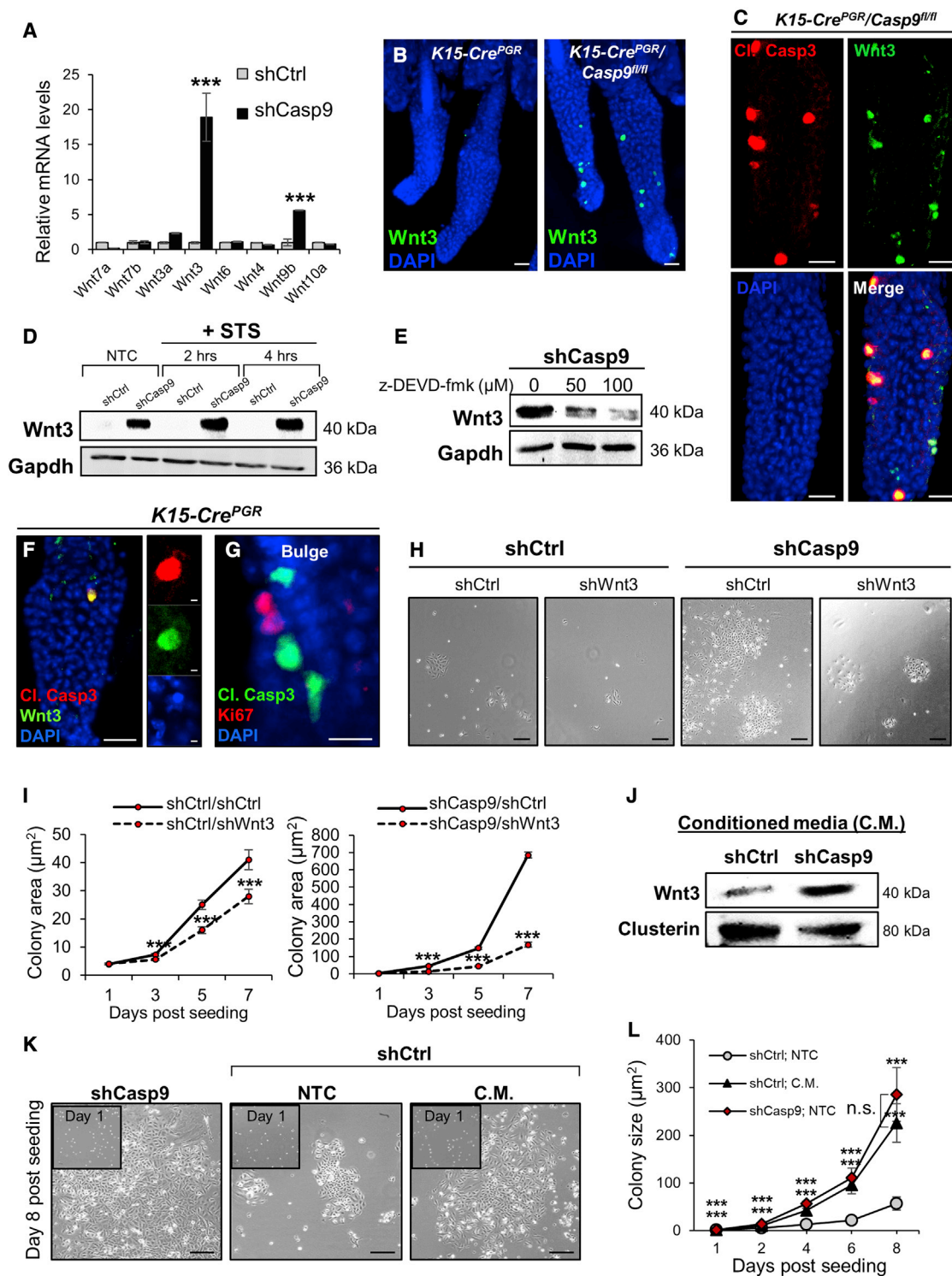


Figure 4. Wnt3 is induced in apoptotic cells

(A) Real-time PCR of different Wnt ligands.
 (B and C) Immunostaining of telogenic HF against Wnt3 (B and C) and cleaved caspase-3 (C).
 (D) Immunoblot of Wnt3 and Gapdh. NTC denotes: non-treated cells.
 (E) Immunoblot of Wnt3 and Gapdh in shCasp9 cells treated with increasing amounts of z-DEVD-fmk.
 (F and G) Co-staining of cleaved caspase-3 with Wnt3 (F) and Ki67 (G) in WT telogenic HF.
 (H) Brightfield images of cells 5 days post-plating.

(legend continued on next page)

with antibodies against Ki67 and cleaved caspase-3. Our results indicated that the majority of proliferating cells (~94%) were localized adjacent to cells positive for cleaved caspase-3, which we have previously shown to mark apoptotic-fated cells (Figures 3L and 3M) (Yosefzon et al., 2018).

Loss of caspase-9 leads to elevated Wnt3 signaling

Our results indicated that caspase-9 can regulate both apoptosis and cell proliferation. In *Drosophila*, pioneering studies have shown that cells undergoing apoptosis can instruct cell proliferation in their vicinity via the AiP mechanism (Huh et al., 2004; Morata et al., 2011; Ryoo et al., 2004). One critical AiP mitogen is Wg, ortholog of mammalian Wnt. In mammals, Wnts regulate the activation of HFSCs (Alonso and Fuchs, 2003; Clevers et al., 2014; Millar et al., 1999). Therefore, we used real-time PCR to examine the induction of different Wnt ligands known to function in the HF (Millar et al., 1999). Our data revealed a ~20-fold increase in the mRNA of the classical Wnt ligand, Wnt3, in shCasp9 HFSCs (Figure 4A). We next examined Wnt3 protein *in vivo* and determined increased level of Wnt3 protein level in specific HFSCs of *K15-Cre^{PGF}/Casp9^{fl/fl}* mice (Figure 4B). We also examined whether these Wnt3-expressing cells were positive for cleaved caspase-3. Performing co-staining experiments, we found that Wnt3 is specifically localized to cleaved caspase-3⁺ cells (Figure 4C). Next, we examined whether Wnt3 is induced upon apoptotic stimulation in HFSCs *in vitro*. Our data indicated a substantial time-dependent increase in Wnt3 levels upon caspase-9 silencing (Figure 4D). These findings attest to the increase in Wnt3 induction upon caspase-9 loss of function, potentially explaining the strong increase in proliferation.

We asked whether the activation of caspase-3 could be responsible for the induction of Wnt3. We treated shCasp9 cells with increasing concentrations of the caspase-3 inhibitor z-DEVD-fmk, which revealed that inhibition of caspase-3 could reverse the increased Wnt3 levels (Figure 4E).

We next examined whether Wnt3 release was only limited to an abnormal apoptotic setting or could also be induced from regular apoptotic HFSCs. WT HFSCs were induced with ABT199, and we performed real-time PCR for Wnt3 mRNA, which revealed a time-dependent elevation in Wnt3 mRNA levels (Figure S5A). This increase was dependent upon caspase-3 activity as caspase-3 inhibition decreased Wnt3 expression (Figure S5B). We also detected regular cleaved caspase-3⁺ apoptotic HFSCs in control telogenic HFs that were positive for Wnt3 expression (Figure 4F). Notably, these cells were in close proximity to neighboring Ki67⁺ proliferating cells (Figure 4G). These findings suggest that Wnt3 release from apoptotic HFSCs is a functional mechanism for maintaining the HFSC pool.

Next, we assessed whether this mechanism was specific to HFSCs or represented a general signaling module. First, we administered ABT199 to HaCaT keratinocytes. Although we could detect bona fide apoptotic cell death, verified via acridine

orange staining and caspase-3 activation (Figures S5C and S5D), Wnt3 levels were not affected (Figure S5E). Similarly, Wnt3 transcription was unaffected in mesenchymal SCs induced with ABT199 (Figure S5F). Taking a complementary strategy, we silenced caspase-9 in J2 fibroblasts at an efficiency of 94% (Figure S5G). In contrast to Casp9-silenced HFSCs, J2 fibroblasts did not exhibit increased Wnt3 levels (Figure S5H). In accordance, silencing Casp9 in J2 fibroblasts led to a completely reversed phenotype from HFSCs, demonstrating delayed proliferation (Figures S5I and S5J).

In resting cells, β -catenin is instructed to undergo proteolysis via the Axin2/APC/GSK-3 β destruction complex (Clevers et al., 2014; Lien and Fuchs, 2014; Millar et al., 1999). Upon ligation of Wnt to its receptor, the destruction complex dissociates, enabling stable β -catenin to translocate to the nucleus. Given the increased Wnt3 levels, we examined β -catenin activation using an antibody against non-phosphorylated β -catenin. In shCasp9 HFSCs, we found a significant increase in the nuclear localization of β -catenin (Figures S5K and S5L). Moreover, we found a significant increase in the mRNA of target genes *cMyc*, *Axin2*, and *CCND1* upon caspase-9 silencing (Figure S5M).

We next examined whether Wnt3 could be responsible for the observed expansion phenotypes seen in shCasp9 cultures. We silenced Wnt3 (denoted shWnt3) in shCtrl and shCasp9 HFSCs and verified decreased Wnt3 protein levels (Figures S5N and S5O). Upon knockdown of Wnt3, a significant decrease was evident in the expansion of both shCtrl and shCasp9 HFSCs (Figures 4H and 4I). Given that Wnt ligands are secreted (Langton et al., 2016), we also isolated conditioned medium (C.M.) from shCtrl and shCasp9 cells and immunoblotted against Wnt3. Our result show that, in contrast to control, shCasp9 cultures release Wnt3 (Figure 4J). To examine whether Wnt3 release is sufficient to induce the HFSC expansion phenotype seen upon caspase-9 silencing, we collected C.M. from shCasp9 cultures and supplemented it to shCtrl cells. When grown in shCasp9-derived C.M., shCtrl cells expanded significantly faster resembling the proliferation kinetics of shCasp9 cells (Figures 4K and 4L). In further support, when we compared C.M. isolated from shCasp9 and shCasp9/shWnt3 culture with shCtrl cells, the expansion achieved with shCasp9 C.M. supplementation was not observed (Figures S5P and S5Q).

Our results reveal a specific HFSC non-autonomous mechanism, whereby dying cells serve as a replenishing SC niche by releasing Wnt3. Furthermore, it reveals that while an apoptotic cell persists and is insufficiently cleared, it can serve as a mitogenic signaling center instructing abnormal proliferation in its vicinity.

Caspase-3-dependent cleavage of Dusp8 results in p38-Mapk-dependent Wnt induction

Although much is known regarding activity of the Wnt signaling pathway, it is still unclear which factors induce the transcription of Wnt ligands. Our results indicate that caspase-3 induces Wnt3

(I) Quantification of colony size.

(J) Proteins extracted from C.M. immunoblotted against Wnt3 and clusterin.

(K) Brightfield images of shCasp9 cells and of cells grown with shCtrl or shCasp9 C.M.

(L) Quantification of colony size of shCasp9 cells and cells grown with shCtrl or shCasp9 C.M.

Images are representative of $n = 3$ mice or ≥ 3 culture triplicates. Error bars represent \pm SEM. Scale bars: 250 μ m (H and K), 20 μ m (C and F), 10 μ m (G).

See also Figure S5.

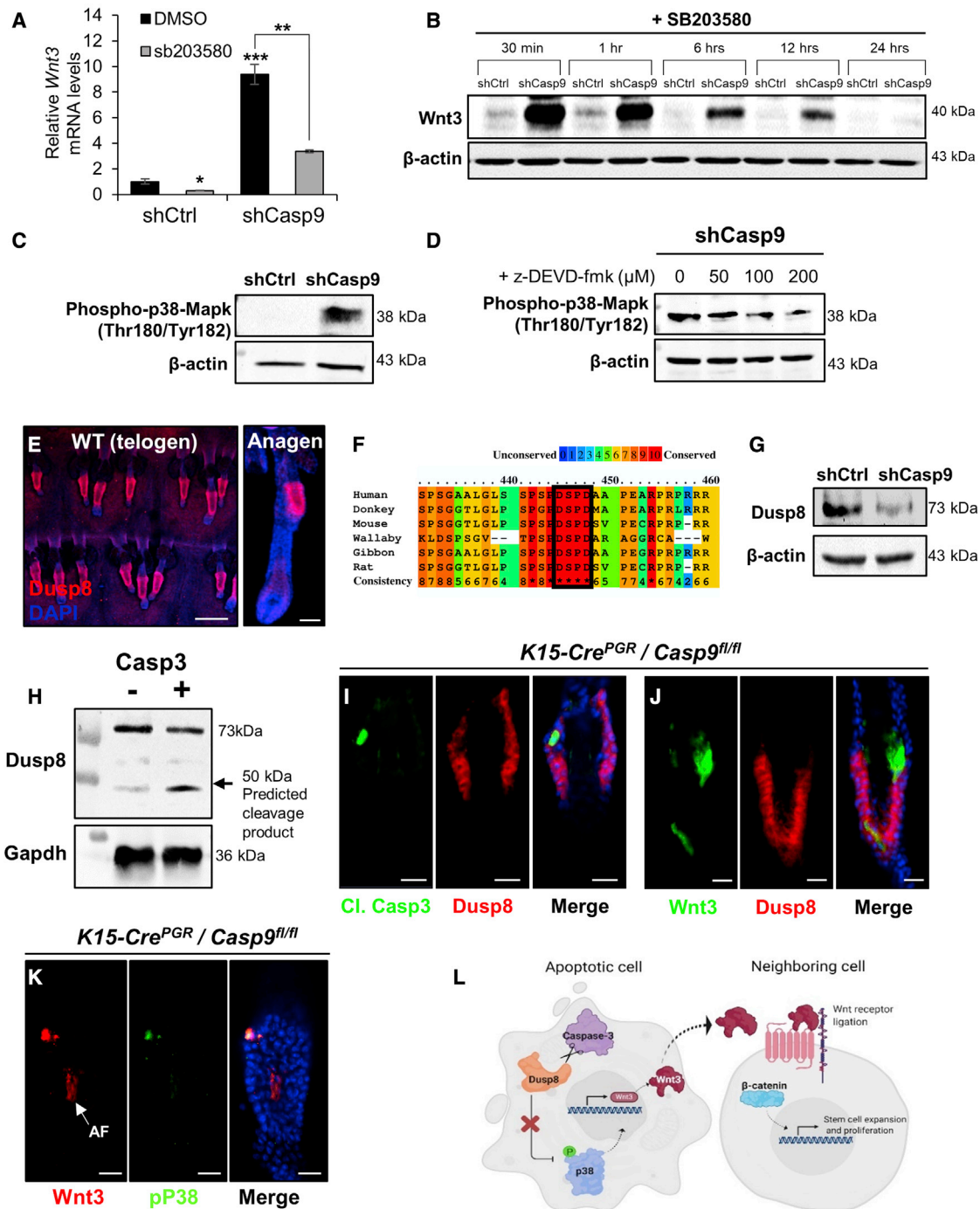


Figure 5. Caspase-3-dependent cleavage of Dusp8 results in p38-Mapk-dependent Wnt induction

(A) Real-time PCR analysis for Wnt3 mRNA upon p38 inhibition (SB203580).
 (B) Immunoblot against Wnt3 and β-actin of cells treated with SB203580.
 (C) Immunoblot using antibody against phospho-p38-Mapk.
 (D) shCasp9 cells treated with increasing concentrations of z-DEVD-fmk and immunoblotted against phospho-p38-Mapk.
 (E) Immunostaining of telogenic tail skin against Dusp8. Right panel shows individual anagenic HF.
 (F) Predicted DUSP8 evolutionary conserved caspase-3 cleavage site.
 (G) Immunoblot of full-length Dusp8 in HFSCs.
 (H) Proteins isolated from CD34⁺ HFSCs subjected to *in vitro* cleavage reaction with cleaved CASPASE-3 and immunoblotted for Dusp8 and Gapdh.
 (I and J) Telogenic tail HF co-stained with Dusp8 and cleaved caspase-3 (I) or Wnt3 (J).
 (K) Telogenic tail HF co-stained for phospho-p38-Mapk and Wnt3.

(legend continued on next page)

upon activation, raising the question of how a cysteine protease could drive the transcription of *Wnt3*.

We hypothesized that the activation of a specific transcription factor was initiated upon cleavage of caspase-3. Taking the initial steps, we utilized various chemical inhibitors of mitogen-activated protein kinase (Mapk) signaling components, which we suspected could regulate *Wnt3* transcription. We administered inhibitors to shCtrl and shCasp9 HFSCs and performed real time-PCR to quantify *Wnt3* mRNA. Our results indicate that inhibition of Erk pathway and Jnk had no effect on the induction of *Wnt3* (Figures S6A and S6B). In contrast, the inhibition of the p38-Mapk cascade, using SB203580, led to a strong decrease in *Wnt3* mRNA in both shCtrl cells and shCasp9 cells (Figure 5A). We verified these findings by culturing shCasp9 HFSCs with SB203580. Within 6 h we detected a robust decrease in *Wnt3* protein levels in both control and shCasp9 HFSCs (Figure 5B). Within 24 h the levels of *Wnt3* were undetectable, indicating a critical role of p38-Mapk in driving the normal transcription of *Wnt3* in HFSCs. Since our data revealed that p38-Mapk is responsible for the induction of *Wnt3* we reasoned that it would become activated upon silencing of caspase-9. Thus, we examined the activation of p38 using specific antibodies for its phosphorylated state, which indicated that p38 is highly phosphorylated in shCasp9 HFSCs *in vitro* (Figure 5C). We next asked whether this effect is mediated by caspase-3. We applied increasing doses of the caspase-3 inhibitor z-DEVD-fmk to shCasp9 cells and detected a steady dose-dependent decrease in phosphorylated p38-Mapk levels (Figure 5D). Since *Wnt3* levels were attenuated by the inhibition of both caspase-3 and p38-Mapk we examined a potential link between these proteins. One physiological inhibitor of p38-Mapk is the dual specific phosphatase 8 (Dusp8) protein (Seternes et al., 2019). As a first step, we examined Dusp8 expression in the epidermis. Our results show that Dusp8 is highly expressed in the HFSC niche in different phases of the HF and can mark the HFSC bulge in both dorsal and tail skins (Figures 5E and S6C).

Considering the specific expression of Dusp8 in the bulge, we hypothesized that active caspase-3 could cleave Dusp8 to enable p38-Mapk hyperactivation. We performed bioinformatic analysis using ScreenCap3 prediction software that revealed that *Dusp8* contains an evolutionary conserved caspase-3 cleavage site with a cleavage probability of 0.98 for the DSPD site (Figure 5F). Next, we examined the levels of full-length Dusp8 *in vitro* and found that the levels of Dusp8 were significantly decreased in shCasp9 HFSCs cells (Figure 5G). To evaluate whether this mechanism also operates in WT HFSCs, we treated HFSCs with ABT199. The induction of cell death in control cells resulted in the reduction of Dusp8 levels consistent with the phosphorylation of p38-Mapk, cleavage of caspase-3 (Figure S6D) and upregulation of *Wnt3* (Figure S5A). We next supplemented recombinant cleaved caspase-3 to protein lysate extracted from HFSCs and immunoblotted against Dusp8. The addition of purified cleaved Caspase-3 resulted in a decrease in the level of full-length Dusp8 (Figure 5H). We identified a novel

band at a molecular weight of ~50 kDa, which correlated to the predicted cleavage site. Although we could barely detect the ~50-kDa fragment in the control sample, a small band could still be seen. We hypothesized that it might be the result of endogenous caspase-3 activity. In support, we could detect the band in whole epidermal lysates (Figure S6E). We verified our findings by performing an *in vitro* cleavage assay utilizing a caspase-3 inhibitor (Ac-DEVD-CHO). Under these conditions the novel band was barely detected (Figure S6F). As a positive control for caspase-3 activation and inhibition we examined cleavage of β -actin (a biochemical target of caspase-3) (Figure S6F; Sokolowski et al., 2014), as well as the negative Gapdh control.

We next performed co-staining against Dusp8, cleaved caspase-3, phosphorylated p38-Mapk, and *Wnt3* in *K15-Cre^{PGR}/Casp9^{fl/fl}* epidermis. Our results indicate diminished Dusp8 levels in HFSCs positive for cleaved caspase-3 (Figure 5I). Furthermore, we found that *Wnt3* was highly increased in cells that expressed low levels of Dusp8 (Figure 5J) and correlated with increased phosphorylated p38-Mapk (Figure 5K).

We also evaluated the effect of Dusp8 silencing in HFSCs. Although silencing was only partially efficient (~40%, Figure S6G), we observed a rise in p38 phosphorylation and *Wnt3* expression (Figures S6H and S6I). Inhibition of caspase-3 in shDusp8 HFSCs cells had no effect on the activation state of p38-Mapk or on *Wnt3* mRNA and protein levels (Figures S6J and S6K). These findings support the epistatic relationship between caspase-3 and Dusp8.

Taken together, our data reveal that Dusp8 is a cleavage target of caspase-3, which attenuates p38-Mapk activation and limits the induction of *Wnt3* in HFSCs (Figure 5L).

Loss of *Casp9* in HFSCs enhances skin repair and HF regeneration

In normal conditions, HFSCs are responsible for fueling the HF cycle and do not contribute to epidermal homeostasis (Ito et al., 2005). However, upon injury, they (and/or progeny) exit their niche to aid in repopulating the epidermis (Ge et al., 2017; Ito et al., 2005; Jensen et al., 2009; Snippert et al., 2010). Since deletion of *Casp9* leads to HFSC expansion, we asked whether it would result in enhanced tissue repair.

We induced early telogenic (P56) mice with RU486 and, following a 3-week period, generated full-thickness punch-biopsy wounds (3 mm²) on the tail, which we monitored for wound coverage (Figures 6A and 6B). In *K15-Cre^{PGR}/Casp9^{fl/fl}* mice, the wound size was reduced by ~30% after 3 days, whereas in control mice no coverage was seen at this time point (Figures 6B and 6C). Accelerated healing was seen at all examined time points in *K15-Cre^{PGR}/Casp9^{fl/fl}* mice (Figure 6C). By 12 days post-wound infliction (PWI), the wounds of both *K15-Cre^{PGR}* and *K15-Cre^{PGR}/Casp9^{fl/fl}* mice had healed (Figure S7A). We also examined whether increased healing could also be seen upon wounding of the dorsal skin. For this aim, we induced mice for Cre recombination followed by infliction of full-thickness excision wounds (1 cm²). The acceleration in re-epithelialization was

(L) Schematic showing caspase-3-mediated cleavage of Dusp8 in a dying cell.

Images are representative of n = 3 mice or ≥ 3 culture triplicates. Error bars represent \pm SEM. Scale bars represent: 200 μ m (E); 20 μ m (I, J, and K). AF denotes autofluorescence.

See also Figure S6.

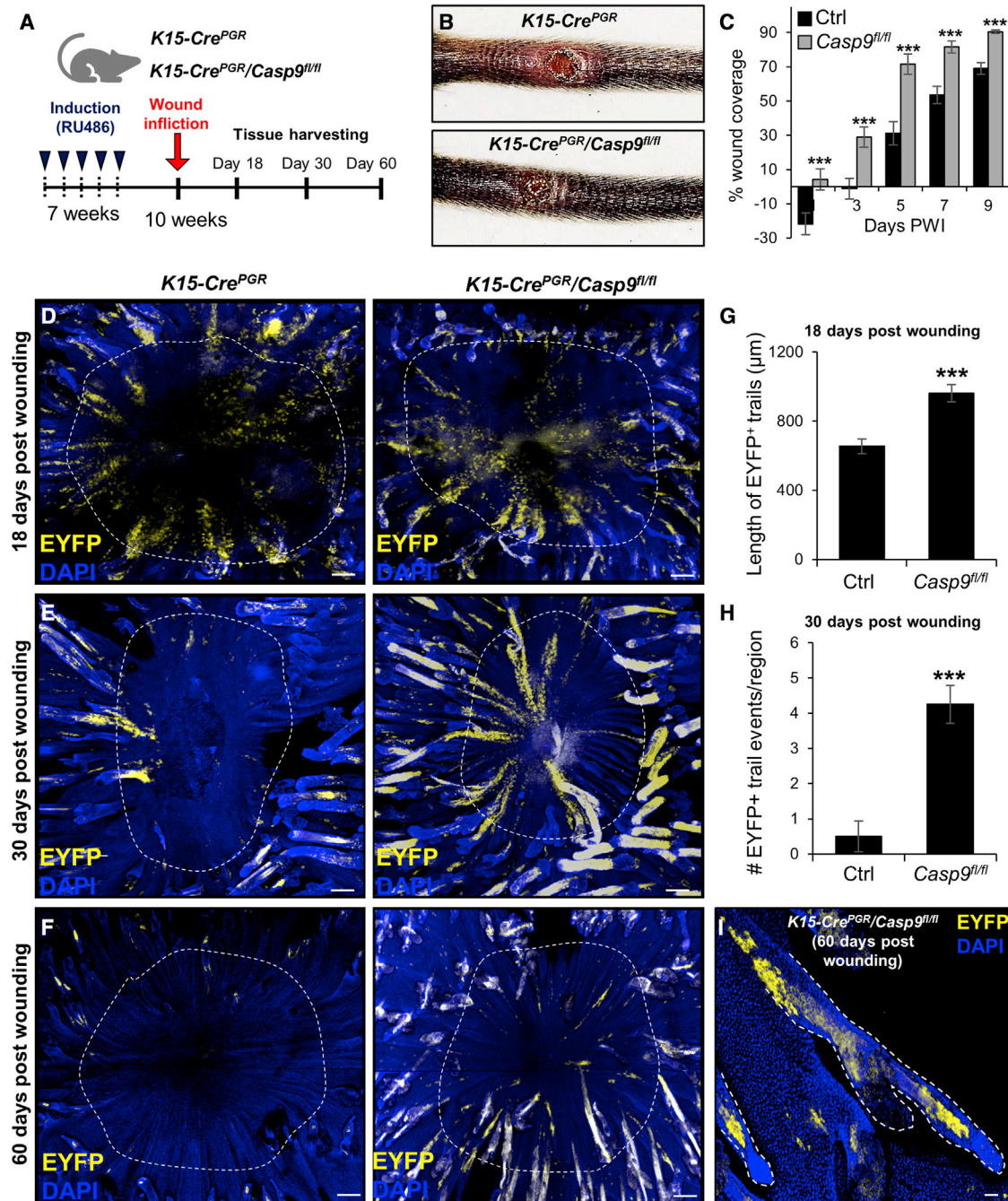


Figure 6. Deletion of *Casp9* in HFSCs results in accelerated SC-dependent wound repair

(A) Experimental outline for *in vivo* wound infliction.
 (B) Photographs of tails wounds at 5 days PWI. Dashed lines represent wound border.
 (C) Quantification of wound closure dynamics.
 (D–F) Lineage tracing analyses at 18 (D), 30 (E), and 60 days PWI (F). Dashed line demarks wound border.
 (G) Length of EYFP⁺ clonal trails at 18 days PWI.
 (H) Number of EYFP⁺ clonal events at 30 days PWI.
 (I) EYFP⁺ trails in a *K15-Cre^{PGR}/Casp9^{fl/fl}* HF in the wound bed at 60 days PWI.
 Images are representative of $n \geq 3$ mice. Error bars represent \pm SEM. Scale bars: 200 μ m (D–F); 100 μ m (I).
 See also [Figure S7](#).

prominent upon *Casp9* deletion in all examined time points (Figures S7B and S7C). These findings are in line with our previous studies showing that upon apoptotic manipulation HFSC lineages are detected next to the wound at early time points (Fuchs et al., 2013).

To investigate the contribution of HFSCs to the accelerated wound repair observed in *Casp9^{fl/fl}* mice we performed lineage tracing using the *Rosa26-EYFP* reporter mice. This was possible since both EYFP⁺ and EYFP⁻ HFSCs expanded proportionally upon *Casp9* deletion, enabling us to assess the contribution of HFSCs to the process.

Since keratin-15 is also expressed in basal interfollicular epidermis (IFE) keratinocytes we carefully examined the presence of EYFP⁺ cells in the epidermis on the first day of wounding. We determined that induction was specific to the HFSCs, since we did not detect EYFP⁺ cells in the IFE (Figure S7D).

At 18 and 30 days post-wounding we observed trails emanating toward the center of the wound in *Casp9*-deleted skins (Figures 6D–6H). Of note, *K15-Cre^{PGR}/Casp9^{fl/fl}* HFSC progeny persisted in the epidermis at 30 and 60 days PWI and were absent in the control. At 60 days PWI we could detect the presence of EYFP⁺ clonal trails specifically emerging from HFSCs toward the wound bed (Figure 6I). We also examined the contribution of immune cells, which could potentially be drawn to apoptotic cells and affect wound repair kinetics. For this, we performed flow cytometry for T and B cells on isolated wounds at 48 h PWI, during the inflammation phase of the wound healing response (Haertel et al., 2014). This analysis indicated no differences in recruitment of the immune response following wounding (Figures S7E and S7F).

During our histological analyses of the wound bed of tail skins, we noted large numbers of newly formed HFSCs within the wound beds of *Casp9^{fl/fl}* tail skins (Figures 7A–7C). We could detect these developing HFSCs at different stages (Figure 7B). These newly formed HFSCs were functionally proliferative as indicated by Ki67 staining within hair buds (Figures 7D and 7E). Additionally, we could detect HFSCs that were positive for EYFP, indicating that *Casp9^{-/-}* HFSCs gave rise to these neogenic HFSCs (Figure 7E). Further examination of the regenerated HFSCs revealed a SC niche that encompassed K15⁺ and Sox9⁺ HFSCs (Figure 7F), indicating that regenerated HFSCs contained functional SCs.

Neogenic HFSCs normally generate unpigmented hair (Ito et al., 2007). Fontana-Masson staining (for melanin) and brightfield images indeed indicated the lack of pigment in these regenerated HFSCs (Figures S7G and S7H). Together, these results suggest that the enhanced expansion of HFSCs seen in *K15-Cre^{PGR}/Casp9^{fl/fl}* mice can contribute to accelerated repair and *de novo* HFSC regeneration following injury.

We next investigated whether the *de novo* HFSC regenerative phenotype seen in the *Casp9^{fl/fl}* mice could be dependent upon Wnt secretion. To this end, we administered the Wnt secretion inhibitor (Wnt-C59) to telogenic mice every second day and inflicted full-thickness wounds on both tail and dorsal skins. At all examined time points we did not detect any effects on healing kinetics (Figures 7G, 7H, S7I, and S7J). This finding is in line with elegant studies showing that Wnts are not required for re-epithelialization but are responsible for *de novo* HFSC regeneration (Ito et al., 2007). Nevertheless, inhibition of Wnt secretion diminished the number of regenerated HFSCs and, in many cases, the wound bed appeared similar to the control (Figures 7I, 7J, S7K).

Taken together, our results indicate that caspase-9 serves as a critical player in HFSC elimination. Furthermore, we found that deletion of *Casp9* confers apoptotic resistance to SCs, thus delaying their clearance and enabling them to continuously secrete Wnt3 to their surroundings. This results in entry of HFSCs into the cell cycle and can facilitate enhanced wound repair and tissue regeneration.

DISCUSSION

Efficient HFSC clearance requires an apoptotic feedforward loop

The classic dogma depicts the orchestration of apoptosis by caspases that are hierarchically organized into the “upstream” initiator and “downstream” executioner caspases that form a linear proteolytic cascade (Thornberry and Lazebnik, 1998).

Our results indicate that although caspase-3 cleavage is delayed *in vitro* upon caspase-9 loss of function, the number of active caspase-3⁺ HFSCs was increased *in vivo*. This raises an intriguing question; why would an initiator caspase be functionally required for apoptosis following the activation of a central executioner caspase?

To answer this question, we utilized *Casp3^{-/-}* mice and found that they did not display any caspase-9 activity in the HF throughout all stages of the cycle. This observation is in line with the finding that human leukemia cell lines deficient for caspase-3 display delayed activation of caspase-9 (McComb et al., 2019). Furthermore, our data suggest that caspase-3 signals back to initiate “upstream” events in order to achieve the threshold required for efficient and rapid clearance of an apoptotic HFSC. These findings are in accordance with elegant studies indicating that the classic linear model insufficiently explains how cells undergo apoptosis (Lakhani et al., 2006; McComb et al., 2019). Specifically, upstream components are amplified through feedback loops initiated by classic “downstream” components in order to achieve the full-blown apoptotic response (Lakhani et al., 2006; McComb et al., 2019). Possibly, the lack of a feedforward loop would potentially prevent the clearance of HFSCs, which in turn answers the question of why the lack of caspase-9 increases the number of active caspase-3⁺ HFSCs.

In accordance with the report that caspase-3 is directly involved in apoptosis-induced lipid scrambling (Segawa et al., 2014; Suzuki et al., 2013), we determined a delay in PS “eat me” signal, as well as decreased cleavage of ATP11C and caspase-3 both *in vitro* and *in vivo*. In complement, the internalization of the phagocytosis repelling molecule, CD47, was delayed upon caspase-9 loss of function. As a result, we observed a strong delay in clearance in functional efferocytosis assays.

Taken together, our results describe an essential amplification circuit, mediated by caspase-9, which is critical for accomplishing full-scale apoptosis in HFSCs and instructing clearance.

Dying cells fuel SC proliferation via a caspase-3/p38/Wnt3 signaling module

For many years, apoptosis had been considered a silent process that does not affect the neighboring environment (Fuchs and Steller, 2015). Our findings indicate that apoptotic HFSCs release Wnt3 to their environment and drive cell proliferation in

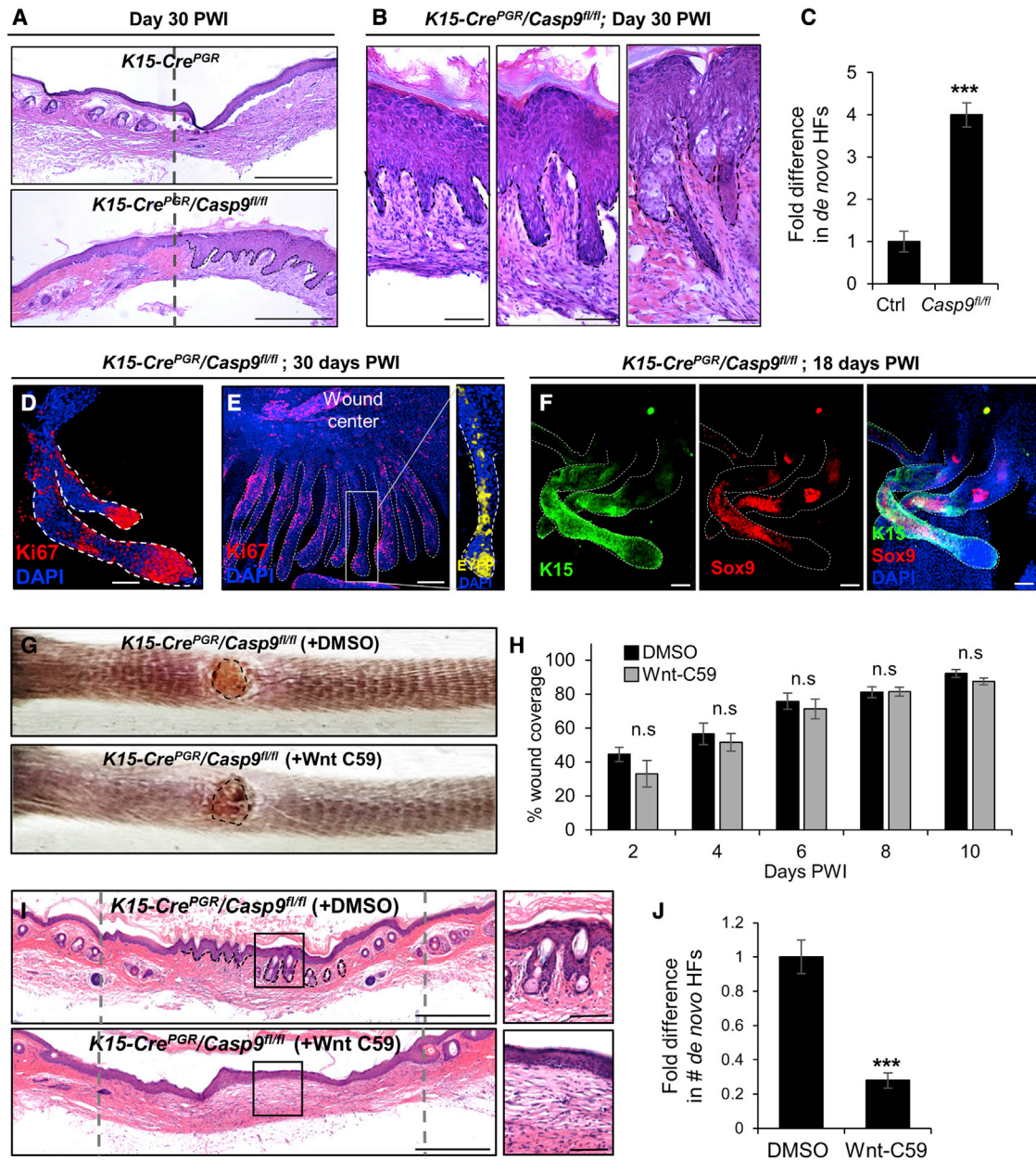


Figure 7. Inhibition of Wnt signaling abrogates HF regeneration in *Casp9^{fl/fl}* mice

(A and B) H&E staining of developing hair pegs, HF and SGs in wound bed of *K15-Cre^{PGR}/Casp9^{fl/fl}* mice 30 days PWI.

(C) Quantification of *de novo* HFs.

(D and E) Staining of *de novo* tail HF with Ki67 at 30 days PWI. Inset of (E) shows single EYFP⁺ regenerated HF.

(F) Tail wound wholemount showing *de novo* HF co-stained with K15 and Sox9 at 18 days PWI.

(G) Photographs of tail wounds treated with DMSO or Wnt-C59 3 days PWI. Dashed lines mark wound area.

(H) Quantification of wound closure dynamics.

(I) H&E staining of wounds treated with DMSO or Wnt-C59. Zoom-in images (right panel).

(J) Quantification of *de novo* HF upon Wnt-C59 administration.

Images are representative of *n* = 6 mice. Error bars represent \pm SEM. Gray dashed lines represent wound border; black dashed lines represent regenerated HF. Scale bars represent: 500 μ m (A); 100 μ m (B); 50 μ m (D, E, E inset, F, G, and G inset).

See also [Figure S7](#).

a manner dependent upon caspase-3 activation. These data are in line with elegant findings in *Drosophila*, which showed that triggering apoptosis in the imaginal wing disc could lead to cell

proliferation and the release of Wg (Wnt ortholog) (Huh et al., 2004; Martín et al., 2009; Morata et al., 2011; Pérez-Garijo et al., 2004; Pérez-Garijo et al., 2009; Ryoo et al., 2004). In

support, additional non-mammalian models have linked cell death-induced-Wnt signaling with tissue regeneration (Brock et al., 2019; Chera et al., 2009).

Our data suggest that *Casp9*-deleted apoptotic cells are preserved in a *Wnt3*-secreting state, akin to overactive niche cells. In *Drosophila*, induction of apoptosis alongside inhibition of executioner caspases locks cells in an “undead” state, where they continue to secrete factors and drive hyperplastic overgrowth (Huh et al., 2004; Pérez-Garijo et al., 2004; Ryoo and Bergmann, 2012; Ryoo et al., 2004). In this context, Dronc (ortholog of caspase-9) is responsible for mitogenic production, while inhibition of Dronc rescues the phenotype (Bosch et al., 2005; Ryoo et al., 2004). Our results indicate that caspase-3 in HFSCs, but not caspase-9, is responsible for *Wnt3* induction.

While much is known regarding Wnt-pathway-regulated gene transcription, the exact molecular steps required for the synthesis and secretion of functional Wnt proteins remain unclear. Our results indicate that the p38-Mapk pathway plays a key role in inducing *Wnt3* transcription. In agreement, various studies have correlated impaired or inhibited p38-MAPK activation to Wnt pathway dysregulation (Cervenka et al., 2011; Hildesheim et al., 2005; Verkaar et al., 2011). In the future it will be key to examine whether p38-Mapk regulates Wnt induction in different tissues and systems.

Deletion of *Casp9* drives wound repair and HF regeneration

We find that mice harboring *Casp9*-deleted $K15^+$ HFSCs displayed rapid re-epithelialization in contrast to control. Although it is widely reported that $K15^+$ HFSCs contribute transiently to epidermal repair (Ito et al., 2005), we noted that the *Casp9*-deleted mice exhibited clonal trails within the epidermis long after wound closure. This observation emphasizes how delayed apoptotic events, mediated by caspase-9, can manifest in uncleared cells that drive tissue regeneration. Previously, it was elegantly demonstrated that Wnt signaling in large excisional epidermal wounds can promote the formation of *de novo* HFs (Ito et al., 2007). Importantly, *de novo* HF regeneration arises from IFE cells and not from cells of HF origin. We found that the absence of caspase-9 results in an increase in regenerated HFs in the wound bed, which could be abrogated upon inhibition of Wnt ligand secretion. Although Wnt is necessary for HF neogenesis, elegant work has shown that signals emanating from the underlying dermis are also required (Lim et al., 2018). It will be key to examine the emanating crosstalk between the dermis and epidermis in *Casp9*^{fl/fl} mice and the manner in which it drives HF neogenesis.

Finally, it should be noted that our observations are not simply limited to caspase-9-manipulated HFSCs. The consequences of communication by dying cells can be detrimental (Ichim and Tait, 2016; Soteriou and Fuchs, 2018; Huang et al., 2011; Kurtova et al., 2015). Given that the majority of cancer therapies eliminate cells by inducing cell death (Soteriou and Fuchs, 2018), it is possible that apoptotic cells might secrete Wnt3 (and/or other mitogens) to elicit an AiP response to replenish the tumor. In the future it will be important to examine AiP in different tumors, determine whether apoptotic cells can serve as a niche for cancer SCs and to establish whether targeting the AiP module can be beneficial for tumor therapy.

Limitations of the study

Although DUSP8 encompasses a caspase-3 cleavage site and we have shown that it is cleaved by caspase-3, it will be beneficial to perform point mutations and mass spectrometry to establish the caspase-3 cleavage site.

STAR★METHODS

Detailed methods are provided in the online version of this paper and include the following:

- KEY RESOURCES TABLE
- RESOURCE AVAILABILITY
 - Lead contact
 - Materials availability
 - Data and code availability
- EXPERIMENTAL MODEL AND SUBJECT DETAILS
 - Mice
 - Cell culture
- METHOD DETAILS
 - Wound repair experiments
 - Depilation experiments
 - Colony formation assays
 - Live imaging
 - Functional phagocytosis assay
 - *In vitro* cleavage assay
 - Flow cytometry
 - RNA extraction, reverse transcription and real-time PCR
 - Immunofluorescence
 - Generation of lentiviral vectors for RNA silencing
 - Protein extraction and western blot
 - RNA sequencing
 - Histology
- QUANTIFICATION AND STATISTICAL ANALYSIS

SUPPLEMENTAL INFORMATION

Supplemental information can be found online at <https://doi.org/10.1016/j.devcel.2021.06.008>.

ACKNOWLEDGMENTS

We apologize to colleagues whose contributions could not be cited due to space constraints. We would like to thank: Fuchs lab members, G. Ventura, L. Voslovizer, X. Velasquez, and I. Maniv. We thank V. Zlobin at the Technion PCRA and E. Barak for flow cytometry. Figure 5L and graphical abstract were generated using BioRender. Work in M.T.L. laboratory was supported by NIH grant R01NS089786. Y.F. was supported by the EMBO Young Investigator program, ICRF (15-771-RCDA) grants, ISF individual 2124/19 and IPMP 1019045-2029637 grants, and ICRF acceleration AG-17-917.

AUTHOR CONTRIBUTIONS

R.A., N.G., Y.Y., E.K., S.B.S., Y.B. and Y.F. designed and performed experiments. M.Y. performed RNA-seq analysis. D.R. and A.F. provided technical assistance with experiments and data analyses. D.J.S. and M.T.L. designed and created the *Casp9*^{fl/fl} mouse. R.A., E.K., and Y.F. wrote the manuscript.

DECLARATION OF INTERESTS

M.T.-L. is a director of Denali Therapeutics and Regeneron Pharmaceuticals. Other authors declare no competing interests.

Received: March 30, 2020
Revised: December 14, 2020
Accepted: June 9, 2021
Published: June 30, 2021

REFERENCES

- Alonso, L., and Fuchs, E. (2003). Stem cells in the skin: waste not, Wnt not. *Genes Dev.* *17*, 1189–1200.
- Alonso, L., and Fuchs, E. (2006). The hair cycle. *J. Cell Sci.* *119*, 391–393.
- Badock, V., Steinhilber, U., Bommert, K., Wittmann-Liebold, B., and Otto, A. (2001). Apoptosis-induced cleavage of keratin 15 and keratin 17 in a human breast epithelial cell line. *Cell Death Differ.* *8*, 308–315.
- Bergmann, A., and Steller, H. (2010). Apoptosis, stem cells, and tissue regeneration. *Sci. Signal.* *3*, re8.
- Blanpain, C., and Fuchs, E. (2009). Epidermal homeostasis: a balancing act of stem cells in the skin. *Nat. Rev. Mol. Cell Biol.* *10*, 207–217.
- Bosch, M., Serras, F., Martín-Blanco, E., and Baguña, J. (2005). JNK signaling pathway required for wound healing in regenerating *Drosophila* wing imaginal discs. *Dev. Biol.* *280*, 73–86.
- Brock, C.K., Wallin, S.T., Ruiz, O.E., Samms, K.M., Mandal, A., Sumner, E.A., and Eisenhoffer, G.T. (2019). Stem cell proliferation is induced by apoptotic bodies from dying cells during epithelial tissue maintenance. *Nat. Commun.* *10*, 1044.
- Červenka, I., Wolf, J., Mašek, J., Krejci, P., Wilcox, W.R., Kozubík, A., Schulte, G., Gutkind, J.S., and Bryja, V. (2011). Mitogen-activated protein kinases promote WNT/beta-catenin signaling via phosphorylation of LRP6. *Mol. Cell Biol.* *31*, 179–189.
- Chera, S., Ghila, L., Dobretz, K., Wenger, Y., Bauer, C., Buzgariu, W., Martinou, J.C., and Galliot, B. (2009). Apoptotic cells provide an unexpected source of Wnt3 signaling to drive hydra head regeneration. *Dev. Cell* *17*, 279–289.
- Clevers, H., Loh, K.M., and Nusse, R. (2014). SC signaling. An integral program for tissue renewal and regeneration: Wnt signaling and SC control. *Science* *346*, 1248012.
- Cotsarelis, G. (2006). Epithelial stem cells: a folliculocentric view. *J. Invest. Dermatol.* *126*, 1459–1468.
- Cotsarelis, G., Sun, T.T., and Lavker, R.M. (1990). Label-retaining cells reside in the bulge area of pilosebaceous unit: implications for follicular stem cells, hair cycle, and skin carcinogenesis. *Cell* *61*, 1329–1337.
- Damgaard, R.B., and Gyrd-Hansen, M. (2011). Inhibitor of apoptosis (IAP) proteins in regulation of inflammation and innate immunity. *Discov. Med.* *11*, 221–231.
- Donepudi, M., and Grütter, M.G. (2002). Structure and zymogen activation of caspases. *Biophys. Chem.* *101–102*, 145–153.
- Fan, Y., and Bergmann, A. (2008). Distinct mechanisms of apoptosis-induced compensatory proliferation in proliferating and differentiating tissues in the *Drosophila* eye. *Dev. Cell* *14*, 399–410.
- Fogarty, C.E., and Bergmann, A. (2017). Killers creating new life: caspases drive apoptosis-induced proliferation in tissue repair and disease. *Cell Death Differ.* *24*, 1390–1400.
- Fogarty, C.E., Diwanji, N., Lindblad, J.L., Tare, M., Amcheslavsky, A., Makhijani, K., Brückner, K., Fan, Y., and Bergmann, A. (2016). Extracellular reactive oxygen species drive apoptosis-induced proliferation via *Drosophila* macrophages. *Curr. Biol.* *26*, 575–584.
- Fuchs, Y., Brown, S., Gorenc, T., Rodriguez, J., Fuchs, E., and Steller, H. (2013). Sept4/Arts regulates stem cell apoptosis and skin regeneration. *Science* *341*, 286–289.
- Fuchs, Y., and Steller, H. (2011). Programmed cell death in animal development and disease. *Cell* *147*, 742–758.
- Fuchs, Y., and Steller, H. (2015). Live to die another way: modes of programmed cell death and the signals emanating from dying cells. *Nat. Rev. Mol. Cell Biol.* *16*, 329–344.
- Ge, Y., Gomez, N.C., Adam, R.C., Nikolova, M., Yang, H., Verma, A., Lu, C.P., Polak, L., Yuan, S., Elemento, O., et al. (2017). Stem cell lineage infidelity drives wound repair and cancer. *Cell* *169*, 636–650.e14.
- Goldstein, J., and Horsley, V. (2012). Home sweet home: skin stem cell niches. *Cell. Mol. Life Sci.* *69*, 2573–2582.
- Green, D.R. (2019). The coming decade of cell death research: five riddles. *Cell* *177*, 1094–1107.
- Gyrd-Hansen, M., and Meier, P. (2010). IAPs: from caspase inhibitors to modulators of NF- κ B, inflammation and cancer. *Nat. Rev. Cancer* *10*, 561–574.
- Haertel, E., Werner, S., and Schäfer, M. (2014). Transcriptional regulation of wound inflammation. *Semin. Immunol.* *26*, 321–328.
- Hakem, R., Hakem, A., Duncan, G.S., Henderson, J.T., Woo, M., Soengas, M.S., Elia, A., de la Pompa, J.L., Kagi, D., Khoo, W., et al. (1998). Differential requirement for caspase 9 in apoptotic pathways in vivo. *Cell* *94*, 339–352.
- Henson, P.M. (2017). Cell removal: efferocytosis. *Annu. Rev. Cell Dev. Biol.* *33*, 127–144.
- Hildesheim, J., Salvador, J.M., Hollander, M.C., and Fornace, A.J., Jr. (2005). Casein kinase 2- and protein kinase A-regulated adenomatous polyposis coli and beta-catenin cellular localization is dependent on p38 MAPK. *J. Biol. Chem.* *280*, 17221–17226.
- Hsu, Y.C., Li, L., and Fuchs, E. (2014). Transit-amplifying cells orchestrate stem cell activity and tissue regeneration. *Cell* *157*, 935–949.
- Hsu, Y.C., Pasolli, H.A., and Fuchs, E. (2011). Dynamics between stem cells, niche, and progeny in the hair follicle. *Cell* *144*, 92–105.
- Hu, Q., Wu, D., Chen, W., Yan, Z., Yan, C., He, T., Liang, Q., and Shi, Y. (2014). Molecular determinants of caspase-9 activation by the Apaf-1 apoptosome. *Proc. Natl. Acad. Sci. U S A* *111*, 16254–16261.
- Huang, Q., Li, F., Liu, X., Li, W., Shi, W., Liu, F.F., O'Sullivan, B., He, Z., Peng, Y., Tan, A.C., et al. (2011). Caspase 3-mediated stimulation of tumor cell repopulation during cancer radiotherapy. *Nat. Med.* *17*, 860–866.
- Huh, J.R., Guo, M., and Hay, B.A. (2004). Compensatory proliferation induced by cell death in the *Drosophila* wing disc requires activity of the apical cell death caspase DRONC in a nonapoptotic role. *Curr. Biol.* *14*, 1262–1266.
- Ichim, G., and Tait, S.W. (2016). A fate worse than death: apoptosis as an oncogenic process. *Nat. Rev. Cancer* *16*, 539–548.
- Ito, M., Liu, Y., Yang, Z., Nguyen, J., Liang, F., Morris, R.J., and Cotsarelis, G. (2005). Stem cells in the hair follicle bulge contribute to wound repair but not to homeostasis of the epidermis. *Nat. Med.* *11*, 1351–1354.
- Ito, M., Yang, Z., Andl, T., Cui, C., Kim, N., Millar, S.E., and Cotsarelis, G. (2007). Wnt-dependent de novo hair follicle regeneration in adult mouse skin after wounding. *Nature* *447*, 316–320.
- Jensen, K.B., Collins, C.A., Nascimento, E., Tan, D.W., Frye, M., Itami, S., and Watt, F.M. (2009). Lrig1 expression defines a distinct multipotent SC population in mammalian epidermis. *J. Cell Sci.* *4*, 427–439.
- Kerr, J.F., Wyllie, A.H., and Currie, A.R. (1972). Apoptosis: a basic biological phenomenon with wide-ranging implications in tissue kinetics. *Br. J. Cancer* *26*, 239–257.
- Kim, H.E., Du, F., Fang, M., and Wang, X. (2005). Formation of apoptosome is initiated by cytochrome c-induced dATP hydrolysis and subsequent nucleotide exchange on Apaf-1. *Proc. Natl. Acad. Sci. U S A* *102*, 17545–17550.
- Koren, E., Yosefzon, Y., Ankawa, R., Soteriou, D., Jacob, A., Nevelsky, A., Ben-Yosef, R., Bar-Sela, G., and Fuchs, Y. (2018). Arts mediates apoptosis and regeneration of the intestinal stem cell niche. *Nat. Commun.* *9*, 4582.
- Kostic, L., Sedov, E., Soteriou, D., Yosefzon, Y., and Fuchs, Y. (2017). Isolation of stem cells and progenitors from mouse epidermis. *Curr. Protoc. Stem Cell Biol.* *41*, 1C.20.1–1C.20.11.
- Kuida, K., Haydar, T.F., Kuan, C.Y., Gu, Y., Taya, C., Karasuyama, H., Su, M.S., Rakic, P., and Flavell, R.A. (1998). Reduced apoptosis and cytochrome c-mediated caspase activation in mice lacking caspase 9. *Cell* *94*, 325–337.
- Kurtova, A.V., Xiao, J., Mo, Q., Pazhanisamy, S., Krasnow, R., Lerner, S.P., Chen, F., Roh, T.T., Lay, E., Ho, P.L., et al. (2015). Blocking PGE2-induced

- tumour repopulation abrogates bladder cancer chemoresistance. *Nature* **517**, 209–213.
- Lakhani, S.A., Masud, A., Kuida, K., Porter, G.A., Jr., Booth, C.J., Mehal, W.Z., Inayat, I., and Flavell, R.A. (2006). Caspases 3 and 7: key mediators of mitochondrial events of apoptosis. *Science* **311**, 847–851.
- Langton, P.F., Kakugawa, S., and Vincent, J.P. (2016). Making, exporting, and modulating Wnts. *Trends Cell Biol.* **26**, 756–765.
- Li, F., Huang, Q., Chen, J., Peng, Y., Roop, D.R., Bedford, J.S., and Li, C.Y. (2010). Apoptotic cells activate the "phoenix rising" pathway to promote wound healing and tissue regeneration. *Sci. Signal.* **3**, ra13.
- Lien, W.H., and Fuchs, E. (2014). Wnt some lose some: transcriptional governance of stem cells by Wnt/beta-catenin signaling. *Genes Dev.* **28**, 1517–1532.
- Lim, C.H., Sun, Q., Ratti, K., Lee, S.H., Zheng, Y., Takeo, M., Lee, W., Rabbani, P., Plikus, M.V., Cain, J.E., et al. (2018). Hedgehog stimulates hair follicle neogenesis by creating inductive dermis during murine skin wound healing. *Nat. Commun.* **9**, 4903.
- Lin, C.F., Chen, C.L., Chang, W.T., Jan, M.S., Hsu, L.J., Wu, R.H., Tang, M.J., Chang, W.C., and Lin, Y.S. (2004). Sequential caspase-2 and caspase-8 activation upstream of mitochondria during ceramide and etoposide-induced apoptosis. *J. Biol. Chem.* **279**, 40755–40761.
- Martín, F.A., Pérez-Garijo, A., and Morata, G. (2009). Apoptosis in *Drosophila*: compensatory proliferation and undead cells. *Int. J. Dev. Biol.* **53**, 1341–1347.
- McComb, S., Chan, P.K., Guinot, A., Hartmannsdottir, H., Jenni, S., Dobay, M.P., Bourquin, J.P., and Bornhauser, B.C. (2019). Efficient apoptosis requires feedback amplification of upstream apoptotic signals by effector caspase-3 or -7. *Sci. Adv.* **5**, eaau9433.
- Mesa, K.R., Rompolas, P., Zito, G., Myung, P., Sun, T.Y., Brown, S., Gonzalez, D.G., Blagoev, K.B., Haberman, A.M., and Greco, V. (2015). Niche-induced cell death and epithelial phagocytosis regulate hair follicle stem cell pool. *Nature* **522**, 94–97.
- Millar, S.E., Willert, K., Salinas, P.C., Roelink, H., Nusse, R., Sussman, D.J., and Barsh, G.S. (1999). WNT signaling in the control of hair growth and structure. *Dev. Biol.* **207**, 133–149.
- Morata, G., Shlevkov, E., and Pérez-Garijo, A. (2011). Mitogenic signaling from apoptotic cells in *Drosophila*. *Dev. Growth Differ.* **53**, 168–176.
- Morris, R.J., Liu, Y., Marles, L., Yang, Z., Trempus, C., Li, S., Lin, J.S., Sawicki, J.A., and Cotsarelis, G. (2004). Capturing and profiling adult hair follicle stem cells. *Nat. Biotechnol.* **22**, 411–417.
- Müller-Röver, S., Handjiski, B., van der Veen, C., Eichmüller, S., Foitzik, K., McKay, I.A., Stenn, K.S., and Paus, R. (2001). A comprehensive guide for the accurate classification of murine hair follicles in distinct hair cycle stages. *J. Invest. Dermatol.* **117**, 3–15.
- Nagata, S. (2018). Apoptosis and clearance of apoptotic cells. *Annu. Rev. Immunol.* **36**, 489–517.
- Peltzer, N., and Walczak, H. (2019). Cell death and inflammation - A vital but dangerous liaison. *Trends Immunol.* **40**, 387–402.
- Pérez-Garijo, A., Martín, F.A., and Morata, G. (2004). Caspase inhibition during apoptosis causes abnormal signalling and developmental aberrations in *Drosophila*. *Development* **131**, 5591–5598.
- Pérez-Garijo, A., Shlevkov, E., and Morata, G. (2009). The role of Dpp and Wg in compensatory proliferation and in the formation of hyperplastic overgrowths caused by apoptotic cells in the *Drosophila* wing disc. *Development* **136**, 1169–1177.
- Rehm, M., Huber, H.J., Dussmann, H., and Prehn, J.H. (2006). Systems analysis of effector caspase activation and its control by X-linked inhibitor of apoptosis protein. *EMBO J.* **25**, 4338–4349.
- Ryoo, H.D., and Bergmann, A. (2012). The role of apoptosis-induced proliferation for regeneration and cancer. *Cold Spring Harb. Perspect. Biol.* **4**, a008797.
- Ryoo, H.D., Gorenc, T., and Steller, H. (2004). Apoptotic cells can induce compensatory cell proliferation through the JNK and the Wingless signaling pathways. *Dev. Cell* **7**, 491–501.
- Sancak, Y., Peterson, T.R., Shaul, Y.D., Lindquist, R.A., Thoreen, C.C., Bar-Peled, L., and Sabatini, D.M. (2008). The Rag GTPases bind raptor and mediate amino acid signaling to mTORC1. *Science* **320**, 1496–1501.
- Segawa, K., Kurata, S., Yanagihashi, Y., Brummelkamp, T.R., Matsuda, F., and Nagata, S. (2014). Caspase-mediated cleavage of phospholipid flippase for apoptotic phosphatidylserine exposure. *Science* **344**, 1164–1168.
- Seternes, O.M., Kidger, A.M., and Keyse, S.M. (2019). Dual-specificity MAP kinase phosphatases in health and disease. *Biochim. Biophys. Acta Mol. Cell Res.* **1866**, 124–143.
- Singh, R., Letai, A., and Sarosiek, K. (2019). Regulation of apoptosis in health and disease: the balancing act of BCL-2 family proteins. *Nat. Rev. Mol. Cell Biol.* **20**, 175–193.
- Snippert, H.J., Haegebarth, A., Kasper, M., Jaks, V., van Es, J.H., Barker, N., van de Wetering, M., van den Born, M., Begthel, H., Vries, R.G., et al. (2010). Lgr6 marks stem cells in the hair follicle that generate all cell lineages of the skin. *Science* **327**, 1385–1389.
- Sokolowski, J.D., Gamage, K.K., Heffron, D.S., Leblanc, A.C., Deppmann, C.D., and Mandell, J.W. (2014). Caspase-mediated cleavage of actin and tubulin is a common feature and sensitive marker of axonal degeneration in neural development and injury. *Acta Neuropathol. Commun.* **2**, 16.
- Soteriou, D., and Fuchs, Y. (2018). A matter of life and death: stem cell survival in tissue regeneration and tumour formation. *Nat. Rev. Cancer* **18**, 187–201.
- Soteriou, D., Kostic, L., Sedov, E., Yosefzon, Y., Steller, H., and Fuchs, Y. (2016). Isolating hair follicle stem cells and epidermal keratinocytes from dorsal mouse skin. *J. Vis. Exp.* **110**, 53931.
- Stennicke, H.R., Jürgensmeier, J.M., Shin, H., Deveraux, Q., Wolf, B.B., Yang, X., Zhou, Q., Ellerby, H.M., Ellerby, L.M., Bredesen, D., et al. (1998). Pro-caspase-3 is a major physiologic target of caspase-8. *J. Biol. Chem.* **273**, 27084–27090.
- Stennicke, H.R., and Salvesen, G.S. (2000). Caspases - controlling intracellular signals by protease zymogen activation. *Biochim. Biophys. Acta* **1477**, 299–306.
- Suzuki, J., Denning, D.P., Imanishi, E., Horvitz, H.R., and Nagata, S. (2013). Xk-related protein 8 and CED-8 promote phosphatidylserine exposure in apoptotic cells. *Science* **341**, 403–406.
- Tadeu, A.M., and Horsley, V. (2014). Epithelial stem cells in adult skin. *Curr. Top. Dev. Biol.* **107**, 109–131.
- Tait, S.W., and Green, D.R. (2013). Mitochondrial regulation of cell death. *Cold Spring Harb. Perspect. Biol.* **5**.
- Thornberry, N.A., and Lazebnik, Y. (1998). Caspases: enemies within. *Science* **281**, 1312–1316.
- Tuzlak, S., Kaufmann, T., and Villunger, A. (2016). Interrogating the relevance of mitochondrial apoptosis for vertebrate development and postnatal tissue homeostasis. *Genes Dev.* **30**, 2133–2151.
- Vanden Berghe, T., Linkermann, A., Jouan-Lanhouet, S., Walczak, H., and Vandenabeele, P. (2014). Regulated necrosis: the expanding network of non-apoptotic cell death pathways. *Nat. Rev. Mol. Cell Biol.* **15**, 135–147.
- Verkaar, F., van der Doelen, A.A., Smits, J.F., Blankesteyn, W.M., and Zaman, G.J. (2011). Inhibition of Wnt/beta-catenin signaling by p38 MAP kinase inhibitors is explained by cross-reactivity with casein kinase I δ/ϵ . *Chem. Biol.* **18**, 485–494.
- Walczak, H. (2011). TNF and ubiquitin at the crossroads of gene activation, cell death, inflammation, and cancer. *Immunol. Rev.* **244**, 9–28.
- Yosefzon, Y., Soteriou, D., Feldman, A., Kostic, L., Koren, E., Brown, S., Ankawa, R., Sedov, E., Glaser, F., and Fuchs, Y. (2018). Caspase-3 regulates YAP-dependent cell proliferation and organ size. *Mol. Cell* **70**, 573–587.e4.

STAR★METHODS

KEY RESOURCES TABLE

REAGENT or RESOURCE	SOURCE	IDENTIFIER
Antibodies		
Krt15	Abcam	Abcam Cat# ab80522; RRID: AB_1603675
ProCaspase-9	Abcam	Abcam Cat# ab2014; RRID: AB_2071321
CD34-eFluor 660	Thermo Fisher Scientific	Cat# 50-0341-82; RRID: AB_10596826
Sca1PE/Cy7	Biolegend	Cat# 108114; RRID: AB_493596
CD49f (Integrin alpha 6) PE	ThermoFisher Scientific	Cat# 12-0495-82; RRID: AB_891474
CD45 APC	Biolegend	Cat# 103112; RRID: AB_312977
CD47 PE	BD Biosciences	Cat# 563585; RRID: AB_2738294
Cleaved PARP1	Cell Signaling	Cat# 9544; RRID: AB_2160724
Cleaved caspase-3	Cell Signaling	Cat# 9664; RRID: AB_2070042
Gapdh	Sigma-Aldrich	Cat# G9545; RRID: AB_796208
Annexin V-iFluor	Abcam	ab219907
Cleaved caspase-8	Cell Signaling	Cat# 8592; RRID: AB_10891784
Ki67	Thermo Fisher Scientific	Cat# 14-5698-82; RRID: AB_10854564
Wnt3	Millipore / Santa Cruz	Cat# 09-162; RRID: AB_11213911/ Cat# sc-74537; RRID: AB_2304409
Sox9	R&D	Cat# AF3075; RRID: AB_2194160
Clusterin	Santa Cruz	Cat# sc-5289; RRID: AB_673566
Dusp8	Abcam	AB184134
Phosphor-p38-Mapk (Thr-180/Tyr182)	Cell Signalling	Cat# 4511; RRID: AB_2139682
β -actin	Santa Cruz	Cat# sc-81178; RRID: AB_2223230
Cleaved caspase-9	Cell Signaling	Cat# 9509; RRID: AB_2073476
ATP11C	Abcam	Cat# ab110710; RRID: AB_10861819
Cytochrome C	Abcam	Cat# ab90529; RRID: AB_10673869
Tom20	Santa Cruz	Cat# sc-17764; RRID: AB_628381
Non-p- β -catenin	Cell Signalling	Cat# 8814; RRID: AB_11127203
Alexa fluor 488	Life Technologies	A11008, A11006, A11001
Alexa fluor 546	Life Technologies	A11010, A11003, A11081
Alexa fluor 633	Life Technologies	A21050, A21070, A21094, A21050
Alexa fluor 594	Life Technologies	A11012, C10246
MitoTracker Red CMXRos	Thermo Fisher	M7512
DAPI	Sigma-Aldrich	D9542
Bacterial and virus strain		
SH5 α competent cells	Thermo Fisher Scientific	#18265017
Chemicals, peptides, and recombinant proteins		
z-DEVD-fmk	AdooQ Bioscience	A13503
Wnt-c59	A2S	A8685
Recombinant human cleaved caspase-3	R&D systems	C3-010-707
ABT199	Active Biochem	A-1231
Staurosporine	Cell Signalling	9953
TNF alpha	Peprtech	315-01A
U0126 (MEK inhibitor)	Sigma-Aldrich	109511-58-2
SP600125 (JNKi)	A2S	A4604-50
SB203580 (p38i)	R&D	1202/10

(Continued on next page)

Continued

REAGENT or RESOURCE	SOURCE	IDENTIFIER
Critical commercial assays		
ApopTag Red In Situ Apoptosis Detection Kit	Millipore	S7165
Experimental models cell lines		
HFSCs	Prof. Yaron Fuchs	N/A
HEK293FT	Thermo Fisher Scientific	R70007
HaCaT	Prof. David Meiri	N/A
3T3-J2	Prof. Hermann Steller	N/A
Raw267.4	Prof. Esther Meyron-Holtz	N/A
Mesenchymal stem cells	Prof. Shulamit Levenberg	N/A
Experimental model: organisms/Strains		
B6;SJL-Tg(Krt1-15-cre/PGR)22Cot/J	Jackson Laboratories	005249
B6.129X1-Gt(ROSA)26Sortm1(EYFP)Cos/J	Jackson Laboratories	006148
Casp9 ^{fl/fl}	Prof. Marc Tessier Lavigne	N/A
C57BL/6J	Envigo	C57BL/6J0laHsd
B6N.129S1-Casp3tm1Flv	Jackson Laboratories	006233
Oligonucleotides		
See Table S1 for complete list of oligonucleotides used in this study		
Recombinant DNA		
pLKO.1 GFP shRNA	Sancak et al. (2008)	Addgene #30323
Pax2	Didier Trono Lab	Addgene #12260
PMD2.G	Didier Trono Lab	Addgene #12259

RESOURCE AVAILABILITY

Lead contact

Further information and requests for resources and reagents should be directed to and will be fulfilled by the lead contact Yaron Fuchs, (yfuchs@technion.ac.il)

Materials availability

Mouse lines generated in this work can be requested from the lead contact's laboratory.

Data and code availability

Caspase gene expression data by RNAseq reported will be shared by the lead contact upon request.

This paper does not report original code.

Any additional information required to reanalyze the data reported in this paper is available from the lead contact upon request.

EXPERIMENTAL MODEL AND SUBJECT DETAILS

Mice

All animal studies were approved by the Committee on the Ethics of Animal Experiments of the Technion, Israel Institute of Technology. Casp3^{tm1Flv} (Casp3^{-/-}), K15-Cre^{PGR} (B6;SJL-Tg(Krt1-15-cre/PGR)22Cot/J) and ROSA26YFP (B6.129X1-Gt(ROSA)26Sortm1(EYFP)Cos/J) were purchased from Jackson Laboratories. Casp9^{fl/fl} mouse was prepared using standard homologous recombination floxing exon 6 surrounding the catalytic region QACGG of Casp9. FRT flanked Neo cassette was inserted between the *LoxP* sites and FLP recombinase was used to remove the Neo cassette. Embryonic stem (ES) cells were targeted with the vector via electroporation. The screening of the ES cells was done by Genentech. K15-Cre^{PGR}/Casp9^{fl/fl} mice were prepared by crossing K15-Cre^{PGR} with Casp9^{fl/fl} mice. Only mice that were Cre positive were used for K15-Cre^{PGR} and K15-Cre^{PGR}/Casp9^{fl/fl} strains and only mice homozygous for the floxed and R26 allele were used for Casp9^{fl/fl}. Experiments were performed on both male and female mice. Littermates of the same sex were randomly assigned to experimental groups. Prior to skin manipulations, mice were shaved with electric clippers and treated topically with hair removal cream (Nair). To activate Cre-recombinase, RU486 was dissolved in DMSO (30mg/ml) and diluted in PBS (1.5 mg/ml). A final concentration of 13.5mg/kg was injected subcutaneously on dorsal skin or at the tip of the tail base. Topical application (30mg/ml RU486 in 80% ethanol)

was applied on dorsal and tail skin. Injections were performed for five consecutive days, skin was harvested at the indicated timepoints. The primers used for genotyping are outlined in [Table S1](#).

Cell culture

HaCaT, HEK293 and Raw264.7 cell lines were cultured in DMEM medium supplemented with 10% FBS, 1% penicillin-streptomycin and 1% L-glutamine. Isolated feeder-free $\alpha 6^+CD34^+$ HFSCs were cultured in HFSC media. HFSC medium was prepared using Dulbecco's modified Eagle medium (DMEM)/F12 3:1 (Biological Industries) containing L-glutamine (Biological Industries; 1:100), penicillin/streptomycin (Biological Industries; 1:100), 10% chelated fetal bovine serum, 5 $\mu\text{g/ml}$ insulin (Sigma I-5500), 5 $\mu\text{g/ml}$ transferrin (Sigma T-2252), 2×10^{-12} M T3 (3,3'-triiodo-L-thyronine; Sigma T-2752), 400 ng/ml hydrocortisone (Sigma H0888), cholera toxin 10–10M and 50mM CaCl_2 . Mesenchymal stem cells were grown in DMEM medium supplemented with 10% FBS, 1% penicillin-streptomycin and 1% L-glutamine, 1% Sodium Pyruvate, and 1% Glutamax. J2 cells were grown in DMEM/F-12 (HAM) 1:1 medium supplemented with 10% FBS, 1% penicillin-streptomycin and 1% L-glutamine. All cells were grown in 37°C, 5% CO_2 . Treatments with Erk pathway inhibitor UO126, Jnk inhibitor SP600125, p38 inhibitor SB203580 (20 μM), z-DEVD-fmk (50, 100, 200 μM , AdooQ Bioscience) or DMSO (as control) were performed for 24 hours. 1 μM of staurosporine (STS), ABT199 (50 μM –200 μM), TNF α /cyclohexamide (20 $\mu\text{g/ml}$, 10 $\mu\text{g/ml}$) were used in cell death assays. For immunofluorescence, cells were fixed in 4% paraformaldehyde for 10 minutes or were harvested for protein or RNA extractions. For Rhodanile staining, cells were incubated with 1% Rhodamine and 1% Nile Blue for 20 minutes and then washed with water. For Acridine orange (AO, Sigma, A6014-10G) staining cells were mixed with a solution of AO and EtBr in PBS and visualized immediately.

METHOD DETAILS

Wound repair experiments

Prior to wounding, eight-weeks old mice were administered RU486 as described above. At 10.5 weeks of age, full-thickness excision wounds (1 cm^2) were inflicted on dorsal skin or 3mm² punch biopsy (Medex Supply) wounds on the tail skin. Wounds were monitored daily and wound size was measured using a transparent sheet. For Wnt-C59 experiments, Wnt-C59 (A2S) was dissolved in DMSO and then in PBS. A final concentration of 2.5mg/kg was injected to each mouse. Injections were performed two days prior to wounding and every other day until mice were sacrificed (day 30 PWI). Mice were sedated with isoflurane during injections and wounding and were administered Buprenorphine (0.1mg/kg) prior to wounding for three days PWI. At the harvesting point, mice were euthanized with CO_2 and the wounded skins were harvested and either embedded in OCT, paraffin or prepared for wholemounts as described below.

Depilation experiments

Prior to depilation, 8-week-old mice were administered with RU486 as described above. At 1-week post induction, waxed strips were used to remove hair from the dorsal skin. Mice were monitored daily for skin coloration changes. At day 8 post depilation, skin was harvested and embedded in OCT for further sectioning and histological staining as described below.

Colony formation assays

Cells were seeded at low confluency (10,000 cells in 35mm plate) and media was changed every two days. For conditional media experiment, media was transferred to target cells on a daily basis. Cells were monitored for colony size and were counted at defined time points.

Live imaging

Cells were treated with STS (1 μM) or ABT199 (50 μM) immediately before the first image was taken. Images were taken every 10 or 15 minutes for 12–24 hours. MitoTracker Red CMXRos (200nM, ThermoFisher) was used to visualize mitochondria during STS treatment. Untreated cells were visualized in the same conditions. IncuCyte live cell analysis system and Zeiss inverted microscope system were used for live imaging. Both systems contain incubator for optimal cell growth conditions (37°C/5% CO_2). Live imaging was performed using a Zeiss inverted microscope or IncuCyte. Movies were merged using VEED- online video editor.

Functional phagocytosis assay

HFSCs were treated with ABT199 (50 μM) for one hour, then washed and treated with 10% normal mouse serum for 20 minutes. Phagocytes (Raw264.7) cells were labelled with CD45-APC by incubation on ice for 10 minutes. Phagocytes were then added to HFSCs at a ratio of 1:10. Time-lapse movies were taken for 12 hours at 10-minute intervals on a Zeiss inverted microscope.

In vitro cleavage assay

Whole cell extracts were prepared as described above and were incubated with recombinant active-CASPASE-3 (100 ng; BD Bioscience) and with Ac-DEVD-CHO (1 μg) at 37°C for three hours in cleavage assay buffer (20 mM PIPES, 100 mM NaCl, 10 mM DTT, 1 mM EDTA, 0.1% (w/v) CHAPS, 10% sucrose, pH 7.2). Reactions were stopped by addition of loading sample buffer and subjected to western blotting.

Flow cytometry

Fluorescent isolated cell sorting (FACS) was performed on a BD FACSAria IIIu utilizing eight-week-old *K15-Cre^{PGR}* and *K15-Cre^{PGR}/Casp9^{fl/fl}* mice that were induced with RU486 as described above. Two days post the final injection, skins were removed, and epidermal tissue digested as previously described (Fuchs et al., 2013). The following antibodies were used: CD34 (1:100), Integrin- α 6 (1:400) and Sca1 (1:200). CD34⁺ population is represented as a percentage from the parental integrin- α 6⁺/Sca1⁻ population. For studies examining cell death kinetics, shCtrl or shCasp9 CD34⁺ cells were treated with ABT199 as described above. Cells were stained with DAPI (500nM) and AnnexinV-647-iFluor (1:200; Abcam) or CD47-PE (1:100). Cells were analyzed on a BD LSR II.

RNA extraction, reverse transcription and real-time PCR

RNA was isolated using TRIzol (Sigma) and up to 2 μ -g of RNA were subjected to cDNA synthesis (Applied Biosystems). Real timePCR was carried out using the PerfeCTa SYBR Green FastMix (Quanta), with gene-specific primers for outlined in [Table S1](#). Amplicon levels were analyzed in triplicates and quantitated relative to a standard curve comprising cDNA. Values were normalized to levels of the housekeeping gene (Rplp0 or Gapdh). Reactions were: 3 min at 95°C, then 40 cycles of 10 sec at 95°C and 30 sec at 60°C with addition of melt curve step: 10 sec at 95°C, and increments of 0.5°C every 5 sec between 65°C to 95°C.

Immunofluorescence

For preparation of wholemount samples, isolated tail and dorsal tissue were treated with 20 mM EDTA for four hours (tail) and six hours (dorsal) at 37°C for efficient separation of the epidermis from the dermis. Following separation, samples were fixed in 4% paraformaldehyde for two hours (tail) or one hour (dorsal) at room temperature. Samples were blocked for two hours in blocking buffer consisting of 10% goat serum, 2% BSA, 0.2% Triton-X. Primary antibodies were diluted in blocking buffer and tissues were incubated overnight at 4°C. Samples were washed at least three times with PBS. Secondary antibodies were incubated for one hour at room temperature followed by four washes with PBS. The following primary antibodies were used: Non-phosphorylated- β -catenin (Rabbit, 1:100, Cell Signaling), Mcm2 (Rabbit, 1:100, Abcam), Procaspase-9 (Rabbit, 1:100, Thermo), Dusp8 (Rabbit, 1:100, Abcam), Wnt3 (Mouse, 1:100, Santa Cruz; Rabbit 1:100 Millipore), cleaved Caspase-3 (Rabbit, 1:100, Cell Signaling), cleaved Caspase-8 (Rabbit, 1:100, Cell Signaling), cleaved Caspase-9 (Rabbit, 1:100, Cell Signaling), Ki67 (Rat, 1:100, eBioscience), Keratin-15 (Mouse, 1:100, Thermo), Sox9 (Rabbit, 1:100, Millipore; Goat, 1:50, Santa Cruz) and CD34 (Rat, 1:100, eBioscience). Antibody staining was visualized using secondary antibodies conjugated to Alexa Fluors dyes: 488, 546, 594, and 633. Additional stains were performed using Terminal deoxynucleotidyl transferase dUTP nick end labeling (TUNEL; ApopTag TdT Millipore kit). Analyses were performed on a Zeiss LSM-880 confocal microscope.

Generation of lentiviral vectors for RNA silencing

To generate lentiviral vectors, we restricted the PLKO.1 lentiviral vector with RsrII and EcoRI enzymes. shRNA oligos were annealed and cloned into PLKO.1 cleaved vector. Sequences were designed by Sigma as follows and our outlined in [Table S1](#).

Plasmids were transfected into HEK293 cells and viruses were collected after one and two days post transfection. Lentiviruses were concentrated and used for infection of various cells using polybrene.

Protein extraction and western blot

Cells were washed with ice-cold PBS and collected by scraping, then centrifugated (4,000 rpm, 5 min at 4°C), lysed in RIPA lysis buffer with protease inhibitor cocktail (Abcam) and then incubated on ice for 30 min. After centrifugation (14,000 rpm, 15 min at 4°C), the proteins (supernatant) were removed and protein concentration was measured (Bradford reagent, BioRad). Protein samples were denatured and resolved on 8% or 12.5 % SDS-PAGE and electrotransferred to a nitrocellulose membrane (Whatman). Membranes were blocked in 5% dry skimmed milk or BSA in TBS-T and incubated with primary antibodies (1:1000). Proteins from conditioned media were extracted using methanol precipitation. The following antibodies were used: Dusp8 (Abcam), Tubulin (Santa Cruz), cleaved Caspase-3 (Cell Signaling), Wnt3 (Millipore), Gapdh (Abcam), cleaved Parp1 (Cell Signaling), ATP11C (Abcam), Clusterin (Santa Cruz), β -actin (Santa Cruz) and Phospho-p38-Mapk (Cell Signaling).

RNA sequencing

α 6^{high}CD34⁺Sca1⁻ and α 6^{high}Sca1⁺ cells were sorted as described earlier. Antibody against Thy1 was utilized to exclude contaminant T-cells and potential interfollicular stem cells. RNA was extracted as described above. Small RNA and mRNA libraries preparation were followed according to the manufacturer's protocols (Illumina Small RNA v1.5 Sample Preparation Kit and Illumina mRNA sequencing Sample Preparation Kit, Illumina). All libraries were sequenced for single-reads, at 100 cycles on the Illumina Genome Analyzer IIx (Illumina). RNA-Seq reads were aligned with STAR aligner against the mouse genome version mm10 and annotated with feature Counts to the Ensembl mm10 gtf annotation. Downstream analysis was performed in R using the DESeq2, ggplots2 and pheatmap packages.

Histology

Isolated dorsal and tail wounds at 18 or 30 days PWI were fixed for two hours (4% PFA). Wounds were embedded in paraffin in the following conditions: 80% EtOH (45 minutes), 95% EtOH (45 minutes x2), 100% EtOH (45 minutes x2), 1:1 EtOH:xylene (45 minutes),

xylene (45 minutes), xylene (30 minutes), paraffin (45 minutes, 54°C, X3) and samples were then embedded in paraffin. Deparaffinization was achieved in the following conditions: xylene (5 minutes, x2), 100% EtOH (2 minutes, x3), 95% EtOH (2 minutes), H₂O wash.

For Hematoxylin and Eosin staining, 7 μ m sections were treated with: Hematoxylin (1 minute; Sigma HHS32), H₂O rinse, differentiator (0.3% alcoholic HCl, 2 dips), H₂O rinse, 95% EtOH (1 minute), Eosin (Sigma, HT110116, 2 minutes), 95% EtOH (10 seconds), 100 EtOH (1 minute, x2), xylene (1 minute, x3). Sections were mounted with xylene-based mounting. Sections were imaged in the biomedical core facility of the Rappaport Faculty of Medicine (Israel).

Fontana-Masson (ab150669) staining was performed according to manufacturing instructions.

QUANTIFICATION AND STATISTICAL ANALYSIS

Data shown are mean \pm SEM. The n values represent biological repeats measured independently as specified in each figure legend. Significance was determined by performing parametric unpaired two-tailed Student's *t* test, where **p* < 0.05, ***p* < 0.01 and ****p* < 0.001. Analysis software include ImageJ and ZEN programs.

Developmental Cell, Volume 56

Supplemental information

**Apoptotic cells represent a dynamic
stem cell niche governing proliferation
and tissue regeneration**

Roi Ankawa, Nitzan Goldberger, Yahav Yosefzon, Elle Koren, Marianna Yusupova, Daniel Rosner, Alona Feldman, Shulamit Baror-Sebban, Yosef Buganim, David J. Simon, Marc Tessier-Lavigne, and Yaron Fuchs

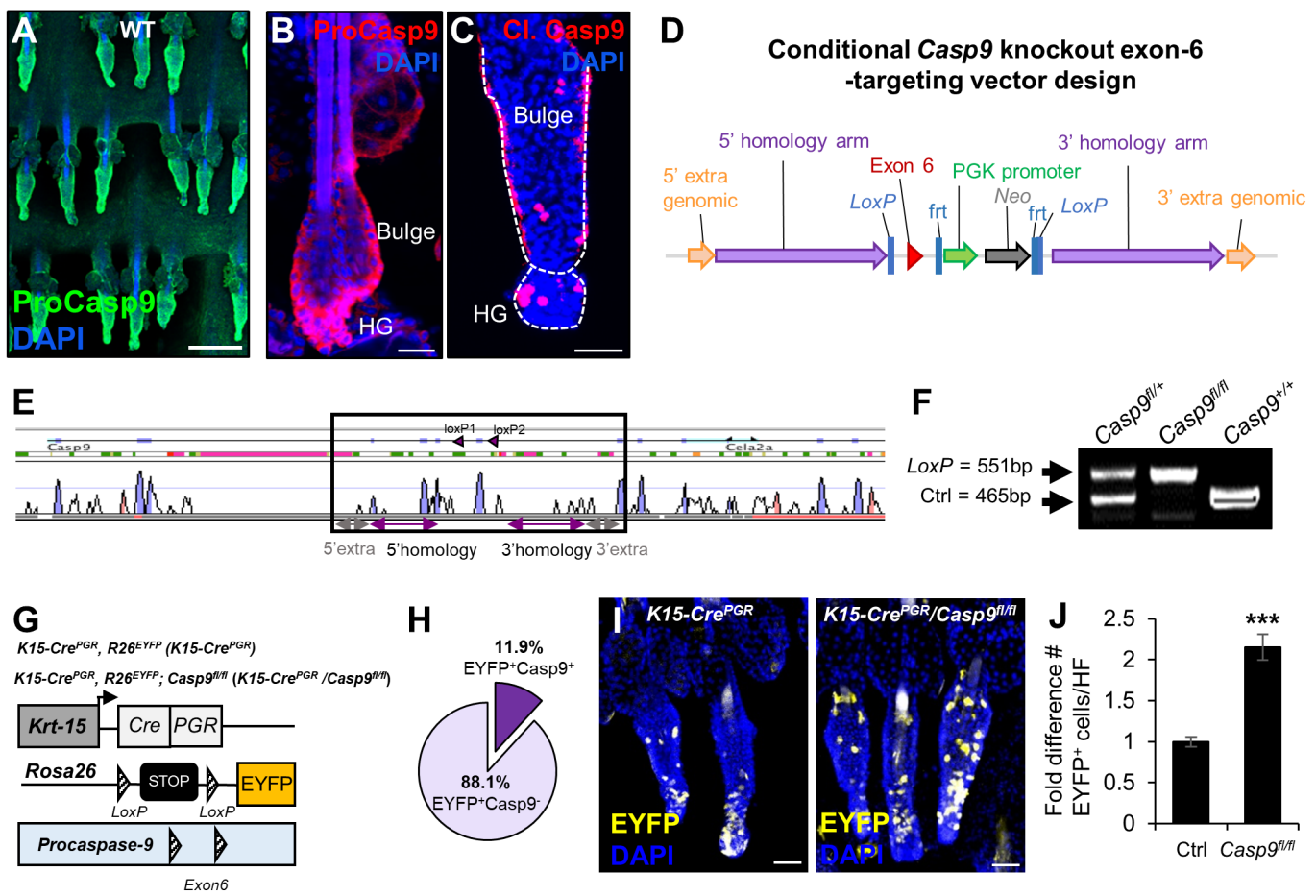


Figure S1. Inducible Caspase-9 deletion in HFSCs results in stem cell niche expansion, related to Figure 1.

(A-B) Immunostaining of procaspase-9 in WT telogenic tail (A) and dorsal (B) interfollicular epidermis.

(C) Immunostaining for cleaved Caspase-9 in WT telogenic tail skin. Dashed line demarcates HFSC niche.

(D) Schematic representation of the targeting vector construct used to create the *Casp9*^{fl/fl} mouse line.

(E) Zoomed-out image of *Casp9* gene with location of *LoxP* site relative to the whole gene.

(F) PCR products of the insertion vector of *K15-Cre*^{PGR}/*Casp9*^{+/+}, *K15-Cre*^{PGR}/*Casp9*^{fl/+}, and *K15-Cre*^{PGR}/*Casp9*^{fl/fl}.

(G) Schematic representation of mouse construct for inducible lineage tracing and conditional deletion of *Casp9*.

(H) Pie chart indicating quantification of EYFP⁺ and pro-Caspase-9⁺ cells (*Casp9*) (n=100 individual HF).

(I) Telogenic HF showing induced EYFP⁺ cells in the tail skin.

(J) Quantification of EYFP⁺ cells per HF unit at one-week post induction (n=100 individual HF).

Data are shown as mean ± SEM. *p < 0.05; **p < 0.01; ***p < 0.001 by two-tailed unpaired Student's t test. Scale bars: 200 μm (A), 50 μm (C, I), 20 μm (B). Denotations: HG; hair germ.

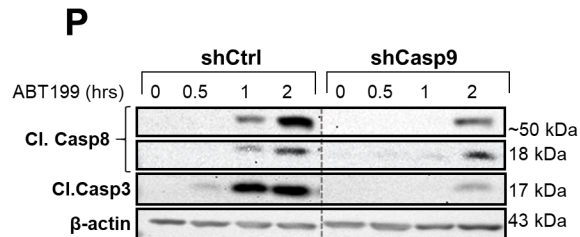
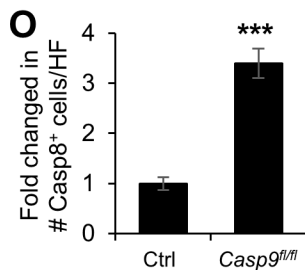
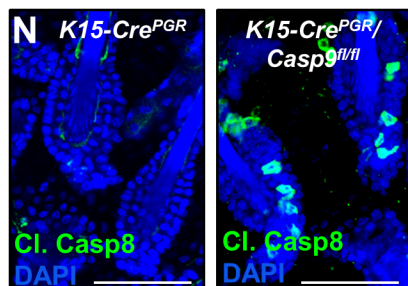
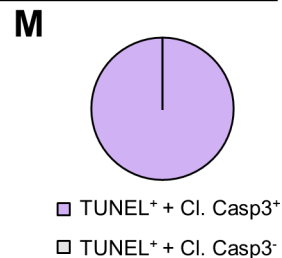
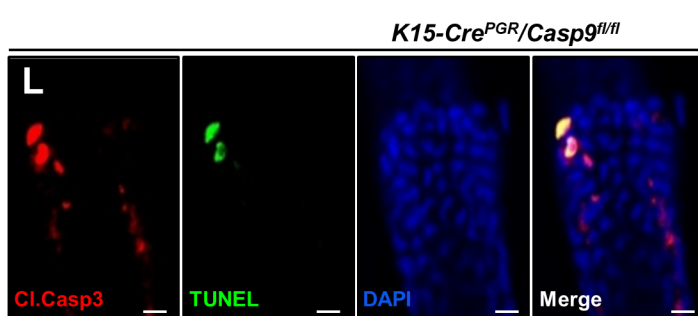
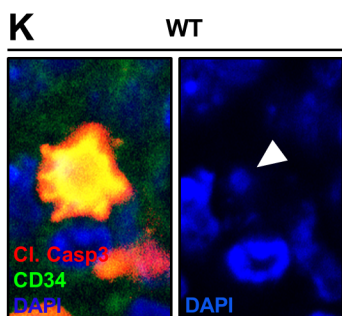
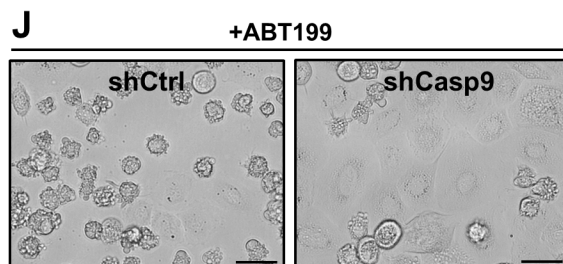
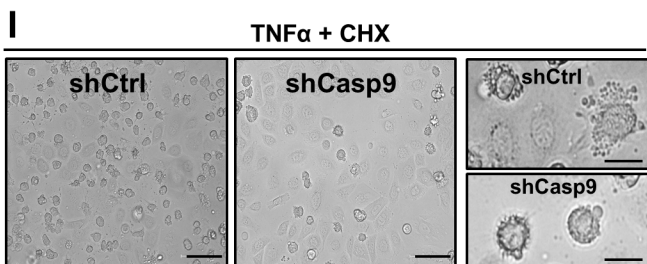
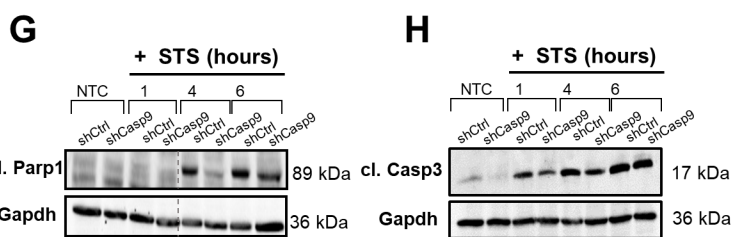
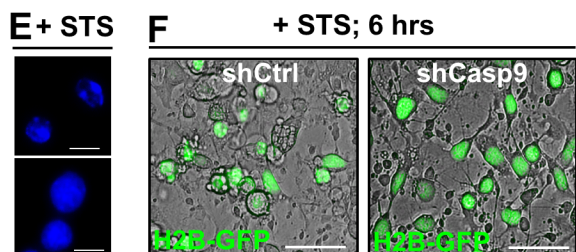
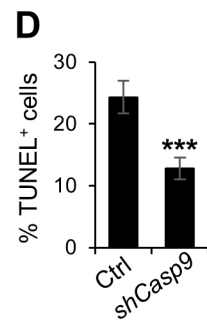
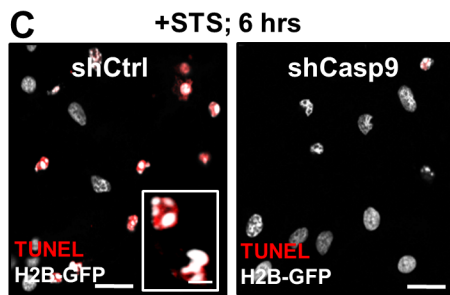
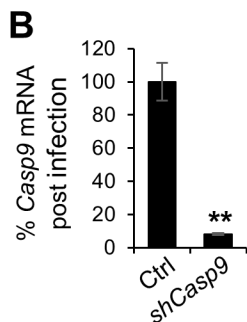
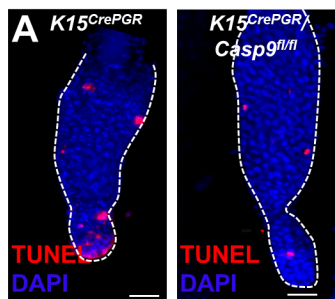


Figure S2. Caspase-9 loss delays apoptosis of HFSCs, related to Figure 2.

- (A) Terminal deoxynucleotidyl transferase dUTP nick end labeling (TUNEL) staining in telogenic HFSCs (HFSCs) from *K15-Cre^{PGR}* and *K15-Cre^{PGR}/Casp9^{fl/fl}* mice. Dashed line demarcates HFSC niche.
- (B) RNA extracts from shCtrl and shCasp9 HFSCs post infection were subjected to real time-PCR analysis for *Casp9* mRNA level quantification (n=3 wells).
- (C) Terminal deoxynucleotidyl transferase dUTP nick end labeling (TUNEL) on shCtrl and shCasp9 cells treated with staurosporine (STS) for six hours. Insets show zoom-in of TUNEL⁺ apoptotic cell displaying condensed nuclear morphology.
- (D) Quantification for TUNEL⁺ cells in shCtrl and shCasp9 cells post STS treatment (n=3 wells).
- (E) Images of DAPI⁺ nuclei of shCtrl and shCasp9 post 6 hours of STS treatment.
- (F) Snapshot brightfield images of shCtrl and shCasp9 post six hours treatment with STS. Nuclei are marked by H2B-GFP.
- (G) shCtrl and shCasp9 treated with STS for increasing time immunoblotted against cleaved-Parp1 and Gapdh. Dashed line indicates exclusion of wells from blot.
- (H) shCtrl and shCasp9 treated with STS for increasing time immunoblotted against cleaved caspase-3 and Gapdh.
- (I) Brightfield images of shCtrl and shCasp9 after four hours treatment with TNF α /cycloheximide. Zoom-in images illustrate apoptotic cell blebbing.
- (J) Brightfield images of shCtrl and shCasp9 treated with ABT199 for two hours.
- (K) Zoom-in image of apoptotic cells stained for cleaved caspase-3 and CD34. Arrowhead points to condensed nucleus showing DAPI single stain.
- (L) Immunostaining of cleaved caspase-3 and TUNEL in *K15-Cre^{PGR}/Casp9^{fl/fl}* telogenic HFSCs.
- (M) Quantification of caspase-3⁺TUNEL⁺ cells *K15-Cre^{PGR}/Casp9^{fl/fl}* telogenic HFSCs (n=100 individual HFSCs).
- (N) Immunostaining of cleaved caspase-8 in *K15-Cre^{PGR}* and *K15-Cre^{PGR}/Casp9^{fl/fl}* telogenic HFSCs.
- (O) Quantification of cleaved caspase-8⁺ cells per HF (n=100 individual HFSCs).
- (P) shCtrl and shCasp9 treated with ABT199 for increasing time immunoblotted against cleaved caspase-3, cleaved caspase-8, and β -actin. Dashed line indicates exclusion of wells from blot.
- Data are shown as mean \pm SEM. *p < 0.05; **p < 0.01; ***p < 0.001 by two-tailed unpaired Student's t test. Scale bars: 55 μ m (F), 50 μ m (N), 43 μ m (J), 25 μ m (I), 20 μ m (A, C), 15 μ m (E), 10 μ m (L).

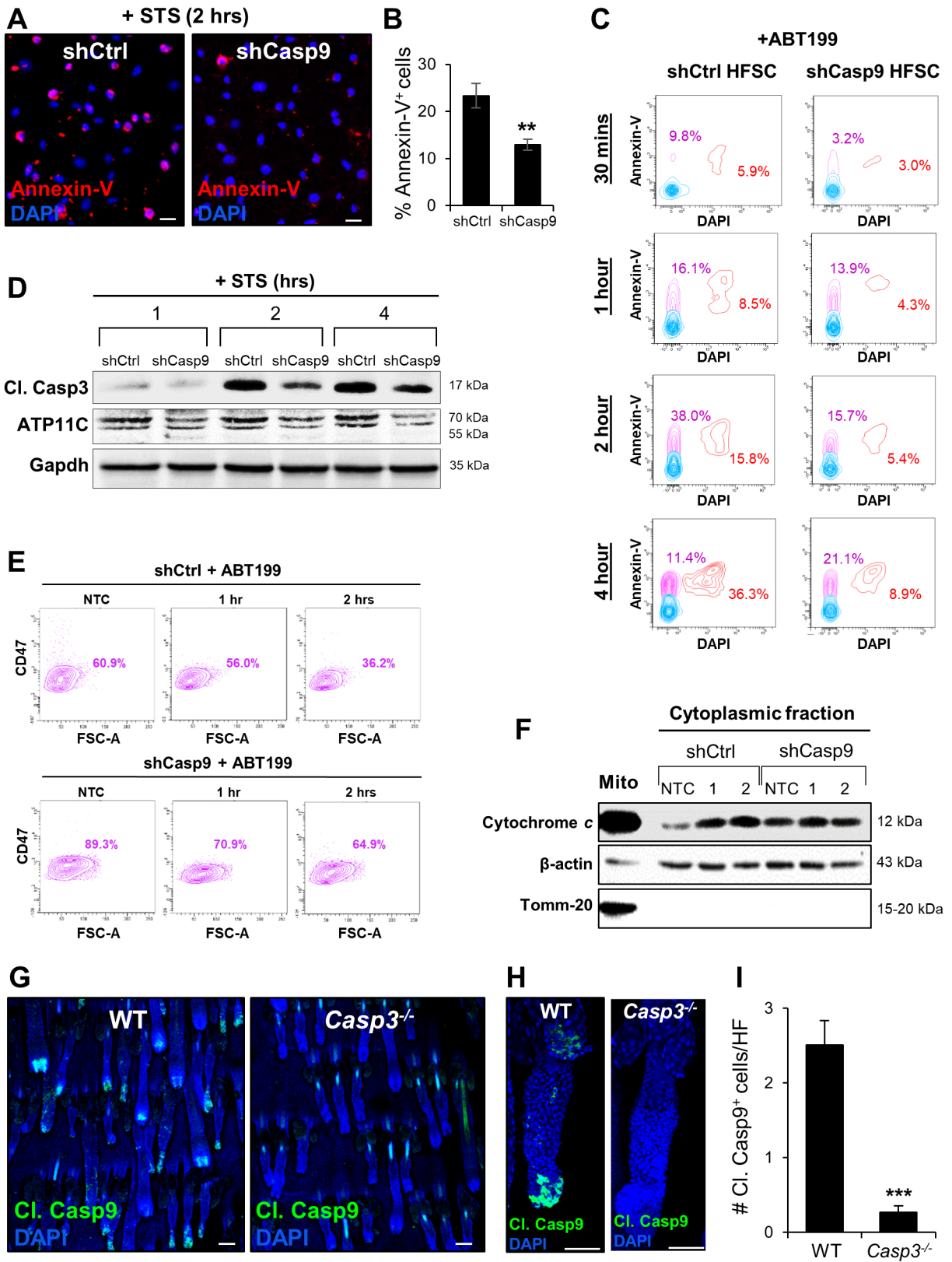


Figure S3. Caspase-9 loss delays clearance of HFSCs, related to Figure 2.

(A) Immunostaining of shCtrl and shCasp9 cells treated with STS for 2 hours and stained with Annexin-V.

(B) Quantification for Annexin-V⁺/DAPI⁺ cells in shCtrl and shCasp9 cells (n=3 wells).

(C) Flow cytometry of Annexin-V against singlets (upper) and DAPI against singlets (lower) at increasing timepoints post ABT199 treatment (n=3 wells).

(D) shCtrl and shCasp9 treated with STS for increasing time immunoblotted against cleaved caspase-3, ATP11C and Gapdh.

(E) Flow cytometric analysis of CD47 against FSC-A following ABT199 treatment for increasing timepoints (n=3 wells).

(F) Cells treated with STS were subjected to mitochondrial fractionation. Cytoplasmic fraction was blotted against cytochrome c, β -actin and Tomm-20. Mitochondria sample was loaded as control for fractionation.

(G and H) Immunostaining of WT and *Casp3*^{-/-} mouse for cleaved caspase-9.

(I) Quantification for number of cleaved caspase-9⁺ cells in WT and *Casp3*^{-/-} mice (n=100 individual HFs).

Data are shown as mean \pm SEM. *p < 0.05; **p < 0.01; ***p < 0.001 by two-tailed unpaired Student's t test. Scale bars: 100 μ m (G), 50 μ m (H), 20 μ m (A).

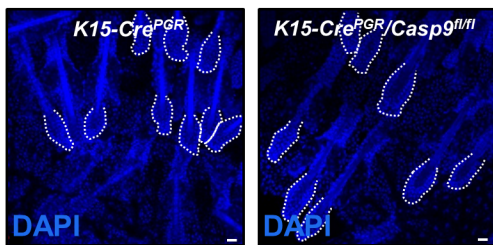
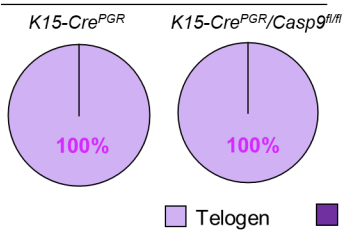
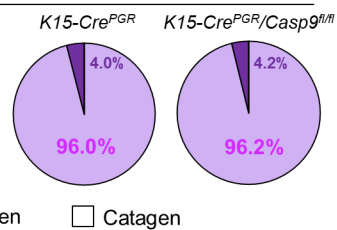
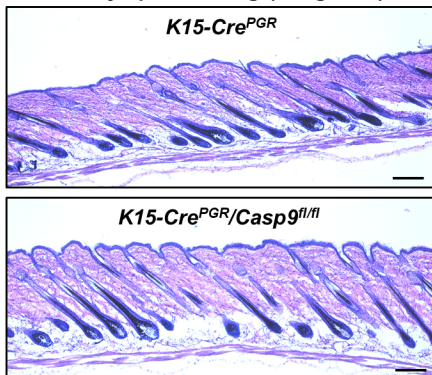
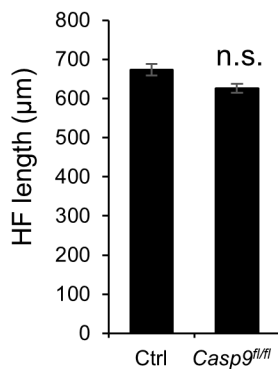
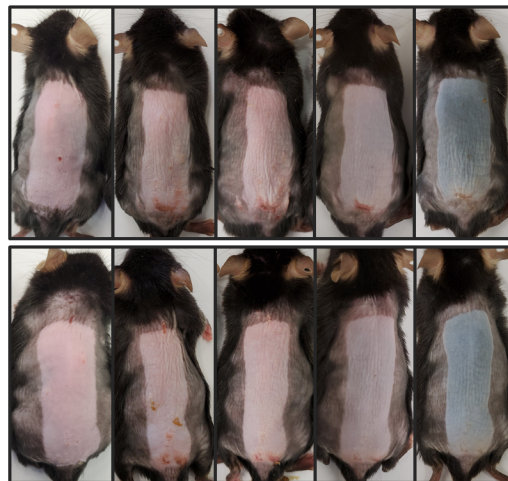
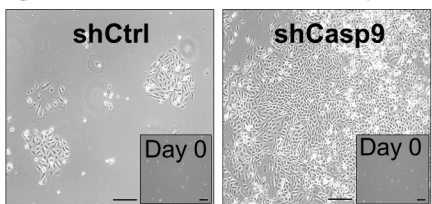
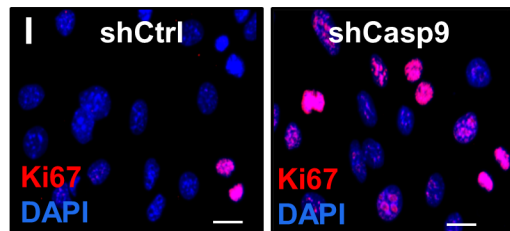
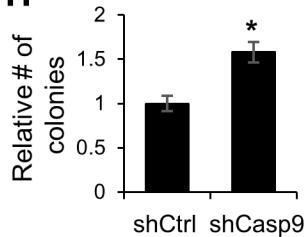
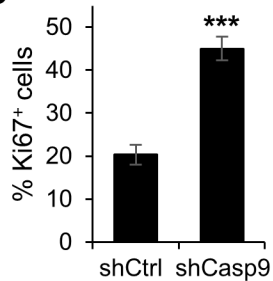
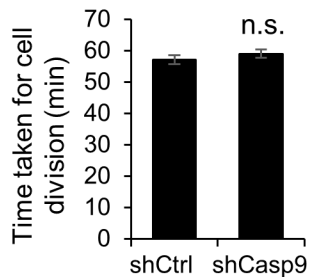
A 3 weeks post induction (PI); 10 weeks old**B** 1 week PI; 8 weeks old**C** 3 weeks PI; 10 weeks old**D** 8 days post waxing (Anagen-VI)**E****F** Day 0 Day 2 Day 4 Day 6 Day 8**G** Cultured CD34⁺ HFSCs; Day 8**H****J****K**

Figure S4. Deletion of *Casp9* results in increased proliferation of HFSCs but does not affect the hair follicle cycle, related to figure 3.

(A) DAPI staining of dorsal HFs from *K15-Cre^{PGR}* and *K15-Cre^{PGR}/*Casp9^{fl/fl}** mice at three weeks post induction (10 weeks old). Dashed line demarcates individual HFs.

(B) Quantification of HF phase in *K15-Cre^{PGR}* and *K15-Cre^{PGR}/*Casp9^{fl/fl}** mice at one week post induction (n=6 mice).

(C) Quantification of HF phase in *K15-Cre^{PGR}* and *K15-Cre^{PGR}/*Casp9^{fl/fl}** mice at three weeks post induction (n=6 mice).

(D) Hematoxylin & Eosin (H&E) staining of dorsal sections from *K15-Cre^{PGR}* and *K15-Cre^{PGR}/*Casp9^{fl/fl}** mice harvested eight days post epilation.

(E) Quantification for anagen length 8 days post epilation (n=6 mice).

(F) Images of *K15-Cre^{PGR}* and *K15-Cre^{PGR}/*Casp9^{fl/fl}** mice at different days post depilation.

(G) Brightfield images of shCtrl and shCasp9 cells at eight days post seeding. Inset shows cell distribution on day one of seeding.

(H) Quantification of daily colony size in shCtrl and shCasp9 (n=3 wells).

(I) Immunostaining of Ki67 in shCtrl and shCasp9⁺ cells.

(J) Quantification for Ki67⁺ cells in shCtrl and shCasp9 cells (n=3 wells).

(K) Quantification for length of mitosis in shCtrl and shCasp9 cells measured from live imaging (n=3 wells).

Data are shown as mean \pm SEM. *p < 0.05; **p < 0.01; ***p < 0.001 by two-tailed unpaired Student's t test. Error bars represent \pm s.e.m. Scale bars: 1000 μ m (D), 250 μ m (F, F inset), 20 μ m (A, H).

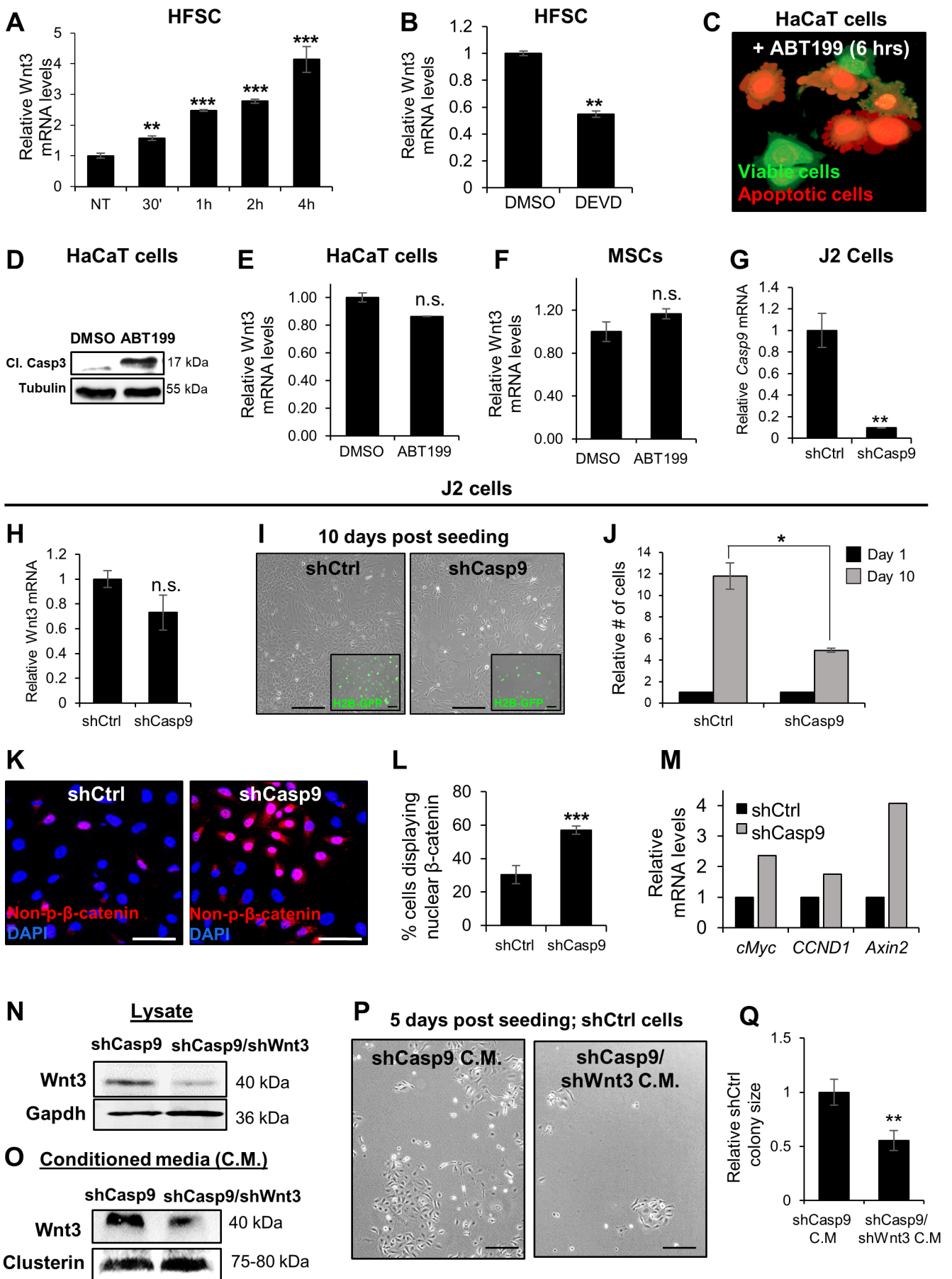


Figure S5. Loss of Caspase-9 in HFSCs leads to elevated Wnt3 signaling, related to Figure 4.

(A) HFSCs treated with ABT199 for increasing timepoints subjected to RT-PCR for *Wnt3* mRNA (n=3 wells).

(B) HFSCs treated with z-DEVD-fmk subjected to real time-PCR for *Wnt3* mRNA (n=3 wells).

(C) Acridine orange staining on HaCaT cells induced after six hours treatment with ABT199.

(D) HaCaT cells treated with ABT199 for six hours immunoblotted against cleaved caspase-3.

(E) HaCaT cells treated with ABT199 for six hours were subjected for real time-PCR analyzing *Wnt3* levels (n=3 wells).

(F) Real time-PCR of mesenchymal SCs (MSCs) treated with ABT199 overnight for *Wnt3* mRNA levels (n=3 wells).

(G) RNA extracts from shCtrl and shCasp9 J2 cells post infection were quantifies for *Casp9* mRNA levels via real time-PCR (n=3 wells).

(H) RNA extracts from shCtrl and shCasp9 J2 cells subjected to real time-PCR to quantify *Wnt3* mRNA levels (n=3 wells).

(I) Brightfield images of shCtrl and shCasp9 J2 cells 10 days post seeding, inset shows H2B-GFP in the cells.

(J) Quantification for relative number of cells at seeding versus 10 days post seeding (n=3 wells).

(K) Immunostaining for nuclear (active) β -catenin in shCtrl and shCasp9 cells.

(L) Quantification for number of shCtrl and shCasp9 cells displaying nuclear β -catenin (n=3 wells).

(M) Real time-PCR for Wnt target genes in shCtrl and shCasp9 cells (n=3 wells).

(N) Proteins isolated from shCasp9 and shCasp9/shWnt3 immunoblotted against Wnt3.

(O) Proteins extracted from conditioned media (C.M.) of shCasp9 and shCasp9/shWnt3 cells immunoblotted against Wnt3.

(P) Representative brightfield images of shCtrl cells treated with shCasp9 or shCasp9/shWnt3 C.M. at five days post seeding.

(Q) Quantification for relative colony size of shCtrl cells at five days post seeding (n=3 wells).

Data are shown as mean \pm SEM. *p < 0.05; **p < 0.01; ***p < 0.001 by two-tailed unpaired Student's t test. Error bars represent \pm s.e.m. Scale bars: 250 μ m (P), 100 μ m (I, I inset), 50 μ m (K).

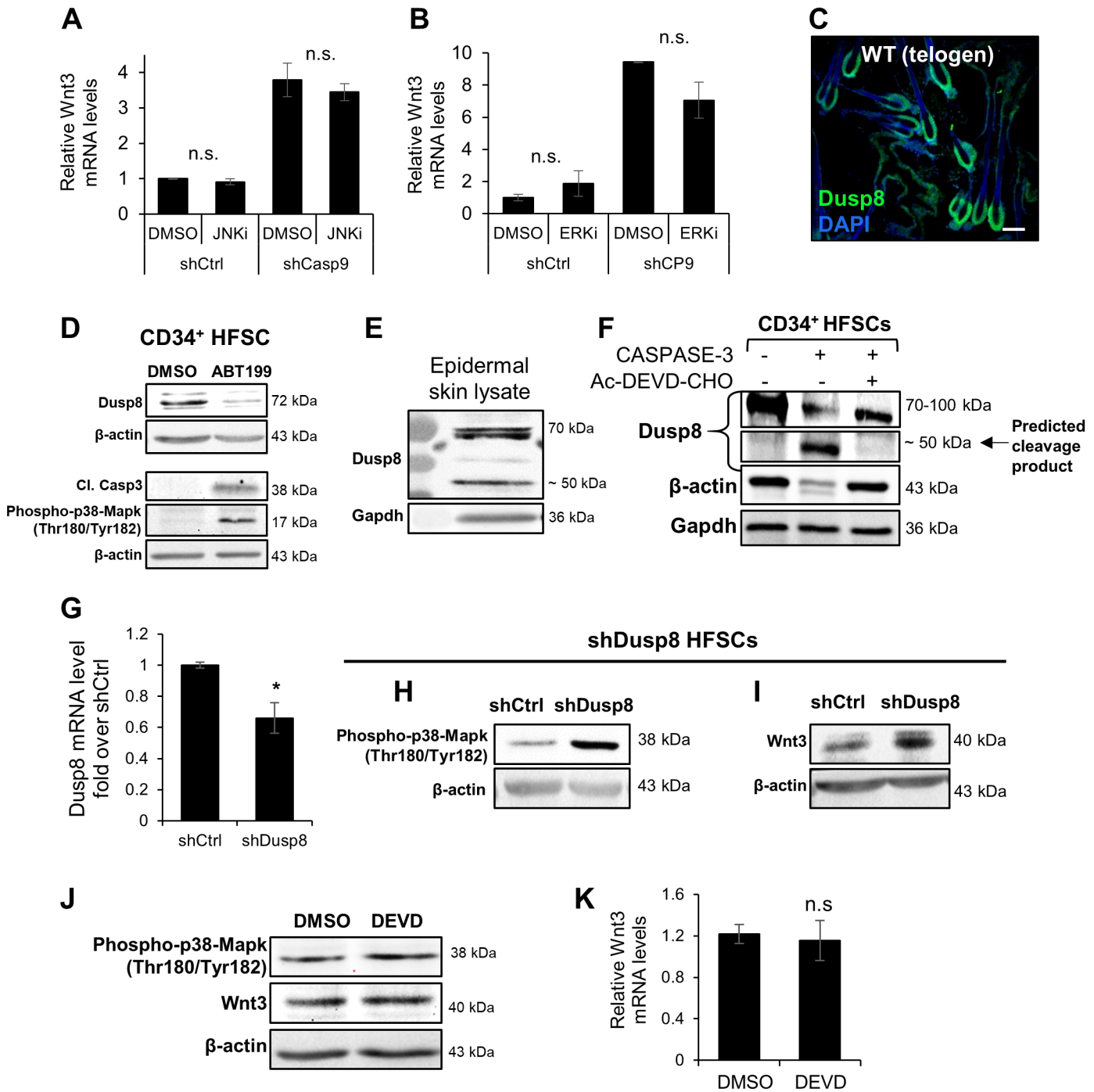


Figure S6. Caspase-3-dependent cleavage of Dusp8 results in p38-Mapk-dependent Wnt3 induction.

Figure S6. Caspase-3-dependent cleavage of Dusp8 results in p38-Mapk-dependent Wnt induction, related to Figure 5.

- (A) Real time-PCR analysis quantifying *Wnt3* mRNA levels in shCtrl and shCasp9 cells treated with JNK inhibitor SP600125 (n=3 wells).
- (B) Real time-PCR analysis of *Wnt3* mRNA in shCtrl and shCasp9 cells treated with ERK pathway inhibitor UO126 (n=3 wells).
- (C) Immunostaining against Dusp8 in WT telogenic dorsal HF.
- (D) Immunoblot of HFSCs treated with ABT199 for one hour immunoblotted with antibodies against Dusp8, cleaved caspase-3, phospho-p38-Mapk and β -actin.
- (E) Immunoblot of whole epidermal lysate blotted for Dusp8 and Gapdh.
- (F) Protein isolated from CD34⁺ HFSCs were subjected to *in vitro* cleavage reaction with human cleaved CASPASE-3 and Ac-DEVD-CHO then immunoblotted for Dusp8, β -actin and Gapdh.
- (G) Real time-PCR of shCtrl and shDusp8 HFSCs for *Dusp8* mRNA levels post infection (n=3 wells).
- (H) Immunoblot of shCtrl and shDusp8 HFSCs with antibodies against phospho-p38-Mapk and β -actin.
- (I) Immunoblot of shCtrl and shDusp8 HFSCs with antibodies against Wnt3 and β -actin.
- (J) shDusp8 HFSCs treated with z-DEVD-fmk and immunoblotted against phospho-p38-Mapk, Wnt3 and β -actin.
- (K) Real time-PCR analysis quantifying *Wnt3* mRNA levels in shDusp8 cells treated with z-DEVD-fmk (n=3 wells).

Data are shown as mean \pm SEM. *p < 0.05; **p < 0.01; ***p < 0.001 by two-tailed unpaired Student's t test. Error bars represent \pm s.e.m. Scale bars: 50 μ m (C).

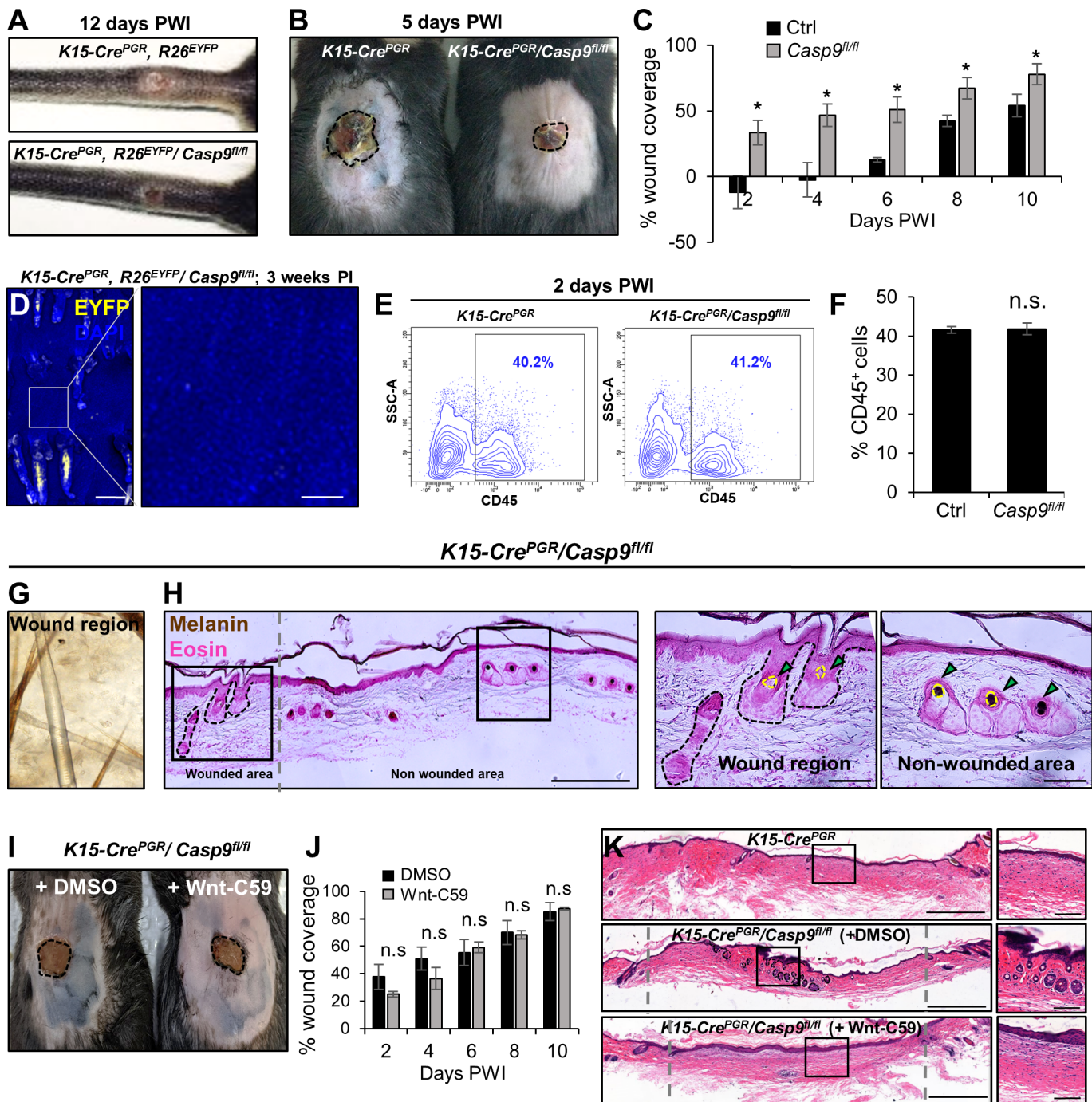


Figure S7. Deletion of *Casp9* in HFSCs results in accelerated SC-dependent wound repair and *de-novo* HF regeneration.

Figure S7. Deletion of *Casp9* in HFSCs results in accelerated SC-dependent wound repair and *de-novo* HF regeneration, related to Figures 6 and 7.

- (A) Tail skin wounds from *K15-Cre^{PGR}* and *K15-Cre^{PGR}/*Casp9*^{fl/fl}* mice at 12 days post wound infliction (PWI).
- (B) Dorsal skin wounds from *K15-Cre^{PGR}* and *K15-Cre^{PGR}/*Casp9*^{fl/fl}* mice at five days PWI.
- (C) Wound closure dynamics measured in *K15-Cre^{PGR}* and *K15-Cre^{PGR}/*Casp9*^{fl/fl}* dorsal wounds (n=6 mice)
- (D) Immunofluorescence image of DAPI and induced EYFP⁺ cells at three weeks post induction.
- (E) Flow analysis of *K15-Cre^{PGR}* and *K15-Cre^{PGR}/*Casp9*^{fl/fl}* dorsal wounds at two days PWI.
- (F) Quantification for CD45⁺ cells from flow cytometry analysis (n=3 wells).
- (G) Brightfield image of white hairs in the *K15-Cre^{PGR}/*Casp9*^{fl/fl}* wounded region.
- (H) Fontana-Masson staining for melanin in *K15-Cre^{PGR}/*Casp9*^{fl/fl}* wounded skin. Dashed line represent individual HFs.
- (I) Dorsal wounds in *K15-Cre^{PGR}/*Casp9*^{fl/fl}* mice treated with DMSO or Wnt-C59 at five days PWI. Dashed line represent wound borders.
- (J) Wound closure dynamics measured in *K15-Cre^{PGR}/*Casp9*^{fl/fl}* (+ DMSO) and *K15-Cre^{PGR}/*Casp9*^{fl/fl}* (+ Wnt-C59) dorsal wounds (n=6 mice).
- (K) Hematoxylin & Eosin (H&E) staining showing *de novo* HF formation in the *K15-Cre^{PGR}, R26^{EYFP}* (+ DMSO) and wound bed.
- Data are shown as mean ± SEM. *p < 0.05; **p < 0.01; ***p < 0.001 by two-tailed unpaired Student's t test. Scale bars: 200 μm (D), (H) 500 μm, 100 μm (K, K insets).